SIAM J. SCI. COMPUT.
Vol. 46, No. 3, pp. A1998–A2024

A NEW LOCALLY DIVERGENCE-FREE PATH-CONSERVATIVE CENTRAL-UPWIND SCHEME FOR IDEAL AND SHALLOW WATER MAGNETOHYDRODYNAMICS*

ALINA CHERTOCK†, ALEXANDER KURGANOV‡, MICHAEL REDLE§, AND KAILIANG WU¶

Abstract. We develop a new second-order unstaggered semidiscrete path-conservative central-upwind (PCCU) scheme for ideal and shallow water magnetohydrodynamics (MHD) equations. The new scheme possesses several important properties: it locally preserves the divergence-free constraint, it does not rely on any (approximate) Riemann problem solver, and it robustly produces high-resolution and nonoscillatory results. The derivation of the scheme is based on the Godunov–Powell nonconservative modifications of the studied MHD systems. The local divergence-free property is enforced by augmenting the modified systems with the evolution equations for the corresponding derivatives of the magnetic field components. These derivatives are then used to design a special piecewise linear reconstruction of the magnetic field, which guarantees a nonoscillatory nature of the resulting scheme. In addition, the proposed PCCU discretization accounts for the jump of the nonconservative product terms across cell interfaces, thereby ensuring stability. We test the proposed PCCU scheme on several benchmarks for both ideal and shallow water MHD systems. The obtained numerical results illustrate the performance of the new scheme, its robustness, and its ability not only to achieve high resolution, but also to preserve the positivity of computed quantities such as density, pressure, and water depth.

Key words. ideal magnetohydrodynamics, shallow water magnetohydrodynamics, divergence-free constraints, path-conservative central-upwind scheme, nonconservative hyperbolic systems of nonlinear PDEs

MSC codes. 65M08, 76W05, 76M12, 86-08, 35L65

DOI. 10.1137/22M1539009

1. Introduction.

This paper focuses on developing a novel numerical method for magnetohydrodynamic (MHD) systems, widely used in many applications, such as astrophysics, plasma physics, space physics, and engineering. In these models, fluid dynamics equations are coupled with the equations for the magnetic field, which satisfies the divergence-free condition—a physically exact constraint, that is, if initially, the divergence of the magnetic field is zero, then it must remain zero for

*Submitted to the journal's Numerical Algorithms for Scientific Computing section December 5, 2022; accepted for publication (in revised form) January 24, 2024; published electronically June 11, 2024.

https://doi.org/10.1137/22M1539009

Funding: The work of the first and third authors was partially supported by National Science Foundation grants DMS-1818684 and DMS-2208438. The work of the second author was partially supported by the National Natural Science Foundation of China through grants 12111530004 and 12171226 and by the Guangdong Provincial Key Laboratory of Computational Science and Material Design through grant 2019B030301001. The work of the fourth author was partially supported by National Natural Science Foundation of China grant 12171227.

†Department of Mathematics and Center for Research in Scientific Computing, North Carolina State University, Raleigh, NC 27695 USA (chertock@math.ncsu.edu).

‡Department of Mathematics, Shenzhen International Center for Mathematics, and Guangdong Provincial Key Laboratory of Computational Science and Material Design, Southern University of Science and Technology, Shenzhen, 518055, China (alexander@sustech.edu.cn).

§Department of Mathematics, North Carolina State University, Raleigh, NC 27695 USA (mtredle@ncsu.edu).

¶Department of Mathematics and Shenzhen International Center for Mathematics, Southern University of Science and Technology, and National Center for Applied Mathematics Shenzhen (NCAMS), Shenzhen, 518055, China (wukl@sustech.edu.cn).

all times. When deriving numerical methods for MHD systems, the divergence-free condition must be handled with care, as neglecting an identically zero divergence on a discrete level may lead to severe numerical instabilities and/or nonphysical structures in the numerical solution; see, e.g., [5, 6, 40, 58]. In addition, like other hyperbolic systems of conservation and balance laws, the MHD systems typically develop very complicated nonsmooth solution structures containing shock waves, rarefactions, and contact discontinuities, as well as their interactions.

In the past few decades, various numerical techniques have been developed to deal with the divergence-free constraint for MHD systems. An early effort in this direction is the projection method [6], which is a postprocessing divergence correction procedure that uses Hodge decomposition to project the non-divergence-free magnetic field into a divergence-free subspace by solving an elliptic Poisson equation. Another widely used approach is the constrained transport (CT) method, which was proposed in [21] for simulating MHD flows. This method preserves a specific discrete version of a divergence-free condition on staggered grids, and its variants were further developed by researchers within various frameworks; see, e.g., [5, 12, 17, 24, 46, 56, 66]. Unstaggered CT methods were also developed (see, e.g., [10, 29, 30, 47, 55]), and they are usually based on numerically evolving the magnetic potential and computing the divergence-free magnetic field through the (discrete) curl of the magnetic potential. In addition, locally divergence-free discontinuous Galerkin methods that enforce the zero divergence of the magnetic field within each cell were developed in [40, 67]. In recent years, globally divergence-free high-order methods were also proposed to enforce the exact zero divergence of the magnetic field within the finite-volume or (central) discontinuous Galerkin framework; see, e.g., [2, 3, 4, 19, 22, 41, 42].

There is also a different class of schemes that reduce the divergence errors but do not explicitly enforce any divergence-free constraint. In the context of the ideal MHD equations, these methods, typically referred to as eight-wave methods, were proposed by Powell et al. [51, 52, 53] based on a proper discretization of a modified, nonconservative ideal MHD model. This model was first introduced by Godunov [26] for entropy symmetrization. Compared to the conservative ideal MHD equations, the modified model contains extra nonconservative source terms (referred to as Godunov–Powell source terms in the following), which are proportional to the divergence of the magnetic field. These source terms change the character of the MHD equations, making the modified model Galilean invariant [14], symmetrizable [26], and better equipped for the design of entropy stable schemes (see, e.g., [9, 16, 45]). In [51], it was also noticed that the conservative ideal MHD equations are weakly hyperbolic, and thus such source terms should be added to recover the missing eigenvector. As demonstrated in [52, 53], the inclusion of the source terms ensures that the magnetic divergence is advected with the flow, and the numerical divergence errors are also expected to be advected and would not accumulate. This makes the eight-wave methods capable of controlling the divergence error, although certain drawbacks may arise due to the nonconservative nature of the Godunov–Powell modified ideal MHD equations; see [58]. As recently discovered in [62], a discrete divergence-free condition is closely related to the positivity-preserving property of numerical schemes for the ideal MHD equations. Furthermore, locally divergence-free positivity-preserving schemes [63, 64] for the Godunov–Powell modified ideal MHD model can be obtained via geometric quasilinearization [65]. Another class of divergence-controlling schemes is the so-called hyperbolic divergence-cleaning method [13], which introduces a mixed hyperbolic-parabolic equation to damp the divergence errors away instead of enforcing an exactly divergence-free magnetic field.

A variant of the MHD equations—known as the shallow water MHD system—has also become a model of significant numerical interest over the last few decades; see,

e.g., [39, 50, 69] and references therein. First introduced in the context of a solar tachocline in [25] and now used in several astrophysical and geophysical contexts, this variant is fully derived from the ideal MHD equations under the assumptions of constant density and magnetohydrostatic equilibrium; see [15, 68]. An assortment of numerical methods have additionally been explored to treat divergence errors for this system—such as space-time conservation element and solution element (CE/SE) methods in [1, 54], an evolution Galerkin scheme in [33], Roe-type schemes with hyperbolic divergence cleaning [32], and entropy-stable schemes in [18, 61], to name a few.

Despite these advances, devising highly accurate, stable, and at the same time robust numerical methods capable of preserving the divergence-free condition at a discrete level is still a challenging task. Our main goal is to develop such a scheme. To this end, we consider the Godunov–Powell modified ideal and shallow water MHD models and supplement them with additional equations obtained by differentiating the magnetic field equations in space; the latter will help to ensure local divergence-free conditions. The resulting augmented MHD systems will be nonconservative and rather complicated to solve using an upwind numerical method, that is, a method relying on a solution of (generalized) Riemann problems. Instead, we numerically solve the augmented MHD systems using second-order unstaggered finite-volume Riemann-problem-solver-free path-conservative central-upwind (PCCU) schemes, which were introduced in [8] as a black-box solver for nonconservative hyperbolic systems of PDEs. PCCU schemes are a path-conservative extension of the central-upwind (CU) schemes, which were developed in [34, 35, 37] for general multidimensional hyperbolic systems of conservation laws. We enforce the local divergence-free condition with the help of a special piecewise linear reconstruction of the magnetic field variables. The resulting scheme produces highly accurate and nonoscillatory results for ideal and shallow water MHD systems.

The paper consists of two parts: In section 2, we study the ideal MHD equations, while section 3 is devoted to the shallow water MHD system. The Godunov–Powell modifications and the augmented forms of the studied systems are presented in sections 2.1 and 3.1, the new numerical methods for the resulting augmented systems are introduced in sections 2.2 and 3.2, and the results of the preformed numerical experiments are reported in sections 2.3 and 3.3. We conclude the paper and discuss some of our future research plans in section 4.

2. Ideal MHD equations.

2.1. Governing equations.

The ideal MHD equations read as

$$\begin{aligned}
&\rho_t+\nabla\cdot(\rho\boldsymbol{u})=0,\\
&(\rho\boldsymbol{u})_t+\nabla\cdot\Big[\rho\boldsymbol{u}\boldsymbol{u}^\top+\Big(p+\frac{1}{2}|\boldsymbol{b}|^2\Big)I-\boldsymbol{b}\boldsymbol{b}^\top\Big]=\boldsymbol{0},\\
&\boldsymbol{b}_t-\nabla\times(\boldsymbol{u}\times\boldsymbol{b})=\boldsymbol{0},\\
&\mathcal{E}_t+\nabla\cdot\Big[\Big(\mathcal{E}+p+\frac{1}{2}|\boldsymbol{b}|^2\Big)\boldsymbol{u}-\boldsymbol{b}(\boldsymbol{u}\cdot\boldsymbol{b})\Big]=0,
\end{aligned}\tag{2.1}$$

where t represents the time, ρ is the density, p is the pressure, $\boldsymbol{u}=(u,v,w)^\top$ represents the fluid velocity, $\boldsymbol{b}=(b_1,b_2,b_3)^\top$ is the magnetic field, and $\mathcal{E}$ is the total energy. Additionally, I is the 3×3 identity matrix, γ represents the ratio of specific heats, and, finally, the system is completed through the equation of state (EOS)

$$\mathcal{E}=\frac{p}{\gamma-1}+\frac{\rho}{2}|\boldsymbol{u}|^2+\frac{1}{2}|\boldsymbol{b}|^2,\tag{2.2}$$

where $|\cdot|$ represents the Euclidean norm. It is easy to show that

$$\nabla \cdot \boldsymbol{b} = 0, \tag{2.3}$$

as long as initially the magnetic field is divergence-free.

As mentioned in section 1, we follow a commonly used approach and, instead of considering (2.1), we develop a new numerical method for the Godunov–Powell modified ideal MHD equations:

$$\begin{aligned}
&\rho_t + \nabla \cdot (\rho \boldsymbol{u}) = 0,\\
&(\rho \boldsymbol{u})_t + \nabla \cdot \Big[\rho \boldsymbol{u}\boldsymbol{u}^\top + \Big(p + \frac{1}{2}|\boldsymbol{b}|^2\Big) I - \boldsymbol{b}\boldsymbol{b}^\top\Big] = -\boldsymbol{b}(\nabla \cdot \boldsymbol{b}),\\
&\boldsymbol{b}_t - \nabla \times (\boldsymbol{u} \times \boldsymbol{b}) = -\boldsymbol{u}(\nabla \cdot \boldsymbol{b}),\\
&\mathcal{E}_t + \nabla \cdot \Big[\Big(\mathcal{E} + p + \frac{1}{2}|\boldsymbol{b}|^2\Big)\boldsymbol{u} - \boldsymbol{b}(\boldsymbol{u} \cdot \boldsymbol{b})\Big] = -(\boldsymbol{u} \cdot \boldsymbol{b})(\nabla \cdot \boldsymbol{b}),
\end{aligned} \tag{2.4}$$

which is closed with the help of the same EOS (2.2). Note that, theoretically, the Godunov–Powell source terms $-\boldsymbol{b}(\nabla \cdot \boldsymbol{b})$, $-\boldsymbol{u}(\nabla \cdot \boldsymbol{b})$, and $-(\boldsymbol{u} \cdot \boldsymbol{b})(\nabla \cdot \boldsymbol{b})$ on the right-hand side (RHS) of (2.4) are zero due to the divergence-free condition (2.3). However, when numerically solving (2.4) with EOS (2.2), these added relaxation terms help to reduce the divergence errors and enhance the robustness; see, e.g., [23, 31, 52, 53, 60, 63, 64]. It is worth noting that although our proposed schemes are locally divergence-free, there are jumps of normal magnetic components across cell interfaces, and the inclusion of these extra source terms can help to control the (weak) divergence errors at cell interfaces.

In this paper, we restrict our attention to the 2-D case, where all the quantities of interest depend on the spatial variables x and y and time t only. In this case, the divergence-free condition (2.3) reads as $(b_1)_x + (b_2)_y = 0$ and one of the goals in the development of a good numerical method for the ideal MHD system (2.4), (2.2) is to enforce this condition at the discrete level. In order to achieve this goal, we introduce the new variables $A := (b_1)_x$ and $B := (b_2)_y$ and differentiate the induction equation for b_1 and b_2 in (2.4) with respect to x and y, respectively, to obtain the following two evolution equations for A and B:

$$\begin{aligned}
&A_t + \big(uA - b_2 u_y\big)_x + \big(vA + b_1 v_x\big)_y = 0,\\
&B_t + \big(uB + b_2 u_y\big)_x + \big(vB - b_1 v_x\big)_y = 0.
\end{aligned} \tag{2.5}$$

From now on, we will add these equations to the Godunov–Powell modified ideal MHD equations and will numerically solve the augmented system (2.4)–(2.5), (2.2). Even though the number of equations to be discretized has been increased, adding the equations in (2.5) makes it easier to control the divergence-free constraint, which now reads as $A + B = 0$.

Before introducing the numerical method, we write the augmented ideal MHD system (2.4)–(2.5) in the following vector form:

$$\boldsymbol{U}_t + \boldsymbol{F}(\boldsymbol{U})_x + \boldsymbol{G}(\boldsymbol{U})_y = Q(\boldsymbol{U})\boldsymbol{U}_x + R(\boldsymbol{U})\boldsymbol{U}_y, \tag{2.6}$$

where $\boldsymbol{U} = (\rho, \rho u, \rho v, \rho w, b_1, b_2, b_3, \mathcal{E}, A, B)^\top$,

$$\begin{aligned}
\boldsymbol{F}(\boldsymbol{U}) = \Big(&\rho u, \rho u^2 + p + \frac{1}{2}|\boldsymbol{b}|^2 - b_1^2, \rho uv - b_1 b_2, \rho uw - b_1 b_3, 0, ub_2 - vb_1,\\
&ub_3 - wb_1, \big(\mathcal{E} + p + \frac{1}{2}|\boldsymbol{b}|^2\big)u - (\boldsymbol{u} \cdot \boldsymbol{b})b_1, uA - b_2 u_y, uB + b_2 u_y\Big)^\top,
\end{aligned} \tag{2.7}$$

$$\begin{aligned}\boldsymbol{G}(\boldsymbol{U}) = \Big(&\rho v, \rho uv - b_1b_2, \rho v^2 + p + \frac{1}{2}|\boldsymbol{b}|^2 - b_2^2, \rho vw - b_2b_3, vb_1 - ub_2, 0,\\ &vb_3 - wb_2, \big(\mathcal{E} + p + \frac{1}{2}|\boldsymbol{b}|^2\big)v - (\boldsymbol{u}\cdot\boldsymbol{b})b_2, vA + b_1v_x, vB - b_1v_x,\Big)^\top,\end{aligned} \tag{2.8}$$

$$Q(\boldsymbol{U}) = \begin{pmatrix} 0&0&0&0&0&0&0&0&0&0\\ 0&0&0&0&-b_1&0&0&0&0&0\\ 0&0&0&0&-b_2&0&0&0&0&0\\ 0&0&0&0&-b_3&0&0&0&0&0\\ 0&0&0&0&-u&0&0&0&0&0\\ 0&0&0&0&-v&0&0&0&0&0\\ 0&0&0&0&-w&0&0&0&0&0\\ 0&0&0&0&-\boldsymbol{u}\cdot\boldsymbol{b}&0&0&0&0&0\\ 0&0&0&0&0&0&0&0&0&0\\ 0&0&0&0&0&0&0&0&0&0 \end{pmatrix}, \tag{2.9}$$

$$R(\boldsymbol{U}) = \begin{pmatrix} 0&0&0&0&0&0&0&0&0&0\\ 0&0&0&0&0&-b_1&0&0&0&0\\ 0&0&0&0&0&-b_2&0&0&0&0\\ 0&0&0&0&0&-b_3&0&0&0&0\\ 0&0&0&0&0&-u&0&0&0&0\\ 0&0&0&0&0&-v&0&0&0&0\\ 0&0&0&0&0&-w&0&0&0&0\\ 0&0&0&0&0&-\boldsymbol{u}\cdot\boldsymbol{b}&0&0&0&0\\ 0&0&0&0&0&0&0&0&0&0\\ 0&0&0&0&0&0&0&0&0&0 \end{pmatrix}. \tag{2.10}$$

2.2. Numerical method. We introduce a uniform Cartesian mesh consisting of the finite-volume cells $C_{j,k} = [x_{j-\frac12}, x_{j+\frac12}] \times [y_{k-\frac12}, y_{k+\frac12}]$ with $x_{j+\frac12} - x_{j-\frac12} \equiv \Delta x$ and $y_{k+\frac12} - y_{k-\frac12} \equiv \Delta y$. We assume that at a certain time level t, the computed solution realized in terms of its cell averages,

$$\overline{\boldsymbol{U}}_{j,k} \approx \frac{1}{\Delta x\Delta y}\iint_{C_{j,k}} \boldsymbol{U}(x,y,t)\,\mathrm{d}x\,\mathrm{d}y,$$

is available. Notice that the dependence of $\overline{\boldsymbol{U}}_{j,k}$ and many other indexed quantities on t is omitted here and throughout the rest of the paper for the sake of brevity.

The cell averages $\overline{\boldsymbol{U}}_{j,k}$ are evolved in time by implementing a dimension-by-dimension extension of the PCCU scheme from [8], which results in the following semidiscretization of (2.6)–(2.10):

$$\begin{aligned}\frac{\mathrm{d}}{\mathrm{d}t}\overline{\boldsymbol{U}}_{j,k} = &-\frac{1}{\Delta x}\Bigg[\boldsymbol{\mathcal{F}}_{j+\frac12,k} - \boldsymbol{\mathcal{F}}_{j-\frac12,k} - \boldsymbol{Q}_{j,k}\\ &- \frac{s^+_{j-\frac12,k}}{s^+_{j-\frac12,k} - s^-_{j-\frac12,k}}\boldsymbol{Q}_{\boldsymbol{\Psi},j-\frac12,k} + \frac{s^-_{j+\frac12,k}}{s^+_{j+\frac12,k} - s^-_{j+\frac12,k}}\boldsymbol{Q}_{\boldsymbol{\Psi},j+\frac12,k}\Bigg]\\ &- \frac{1}{\Delta y}\Bigg[\boldsymbol{\mathcal{G}}_{j,k+\frac12} - \boldsymbol{\mathcal{G}}_{j,k-\frac12} - \boldsymbol{R}_{j,k}\\ &- \frac{s^+_{j,k-\frac12}}{s^+_{j,k-\frac12} - s^-_{j,k-\frac12}}\boldsymbol{R}_{\boldsymbol{\Psi},j,k-\frac12} + \frac{s^-_{j,k+\frac12}}{s^+_{j,k+\frac12} - s^-_{j,k+\frac12}}\boldsymbol{R}_{\boldsymbol{\Psi},j,k+\frac12}\Bigg].\end{aligned} \tag{2.11}$$

Here,

$$\begin{aligned}\boldsymbol{\mathcal{F}}_{j+\frac12,k}&=\frac{s^+_{j+\frac12,k}\boldsymbol{F}\big(\boldsymbol{U}^{\rm E}_{j,k}\big)-s^-_{j+\frac12,k}\boldsymbol{F}\big(\boldsymbol{U}^{\rm W}_{j+1,k}\big)}{s^+_{j+\frac12,k}-s^-_{j+\frac12,k}}\\&\quad+\frac{s^+_{j+\frac12,k}s^-_{j+\frac12,k}}{s^+_{j+\frac12,k}-s^-_{j+\frac12,k}}\Big(\boldsymbol{U}^{\rm W}_{j+1,k}-\boldsymbol{U}^{\rm E}_{j,k}\Big),\\\boldsymbol{\mathcal{G}}_{j,k+\frac12}&=\frac{s^+_{j,k+\frac12}\boldsymbol{G}\big(\boldsymbol{U}^{\rm N}_{j,k}\big)-s^-_{j,k+\frac12}\boldsymbol{G}\big(\boldsymbol{U}^{\rm S}_{j,k+1}\big)}{s^+_{j,k+\frac12}-s^-_{j,k+\frac12}}\\&\quad+\frac{s^+_{j,k+\frac12}s^-_{j,k+\frac12}}{s^+_{j,k+\frac12}-s^-_{j,k+\frac12}}\Big(\boldsymbol{U}^{\rm S}_{j,k+1}-\boldsymbol{U}^{\rm N}_{j,k}\Big)\end{aligned}\tag{2.12}$$

are the CU numerical fluxes from [38], $\boldsymbol{U}^{\rm E,\,W,\,N,\,S}_{j,k}$ are the reconstructed point values at the cell interfaces of cell $C_{j,k}$ (see section 2.2.1 for details), $s^{\pm}_{j+\frac12,k}$ and $s^{\pm}_{j,k+\frac12}$ are the one-sided local speeds of propagation in the x- and y-directions, respectively (see section 2.2.2 for details), and $\boldsymbol{Q}_{j,k}$, $\boldsymbol{R}_{j,k}$, $\boldsymbol{Q}_{\boldsymbol{\Psi},j+\frac12,k}$, and $\boldsymbol{R}_{\boldsymbol{\Psi},j,k+\frac12}$ denote the discretizations of the nonconservative products on the RHS of (2.6) (see section 2.2.3 for details).

We point out that (2.11) is a system of ODEs, which should be numerically integrated in time by an appropriate ODE solver. In the numerical experiments reported in section 2.3, we have used the explicit three-stage third-order strong stability preserving (SSP) Runge–Kutta method; see, e.g., [27, 28]; and, to ensure stability, we meet the following CFL condition:

$$\Delta t\le\eta\cdot\min\left(\frac{\Delta x}{\max\limits_{j,k}\Big\{s^+_{j+\frac12,k},s^-_{j+\frac12,k}\Big\}},\frac{\Delta y}{\max\limits_{j,k}\Big\{s^+_{j,k+\frac12},s^-_{j,k+\frac12}\Big\}}\right),\tag{2.13}$$

where η denotes the CFL number, which must not exceed a value of 0.5. This is a standard CFL restriction for the CU schemes. However, in order to ensure the positivity of the computed values of ρ (and h in the shallow water system considered in section 3 below) one needs to take a smaller CFL number $\eta=0.25$; see, e.g., [36].

2.2.1. Piecewise linear reconstruction. Equipped with the cell averages $\overline{\boldsymbol{U}}_{j,k}$, we first use the EOS (2.2) and compute the approximate point values of u, v, w, and p at the cell centers:

$$\begin{aligned}&u_{j,k}=\frac{(\overline{\rho u})_{j,k}}{\overline{\rho}_{j,k}},\quad v_{j,k}=\frac{(\overline{\rho v})_{j,k}}{\overline{\rho}_{j,k}},\quad w_{j,k}=\frac{(\overline{\rho w})_{j,k}}{\overline{\rho}_{j,k}},\\&p_{j,k}=(\gamma-1)\left[\overline{\mathcal{E}}_{j,k}-\frac12\,\overline{\rho}_{j,k}\left(u^2_{j,k}+v^2_{j,k}+w^2_{j,k}\right)-\frac12\Big((\overline{b_1})^2_{j,k}+(\overline{b_2})^2_{j,k}+(\overline{b_3})^2_{j,k}\Big)\right].\end{aligned}$$

We then introduce a new set of discrete variables,

$$\boldsymbol{W}_{j,k}:=(\overline{\rho}_{j,k},u_{j,k},v_{j,k},w_{j,k},(\overline{b_1})_{j,k},(\overline{b_2})_{j,k},(\overline{b_3})_{j,k},p_{j,k},\overline{A}_{j,k},\overline{B}_{j,k})^\top,$$

and compute the cell interface point values $\boldsymbol{W}^{\rm E,\,W,\,N,\,S}_{j,k}$ using a proper conservative piecewise linear reconstruction,

$$\widetilde{\boldsymbol{W}}(x,y)=\boldsymbol{W}_{j,k}+(\boldsymbol{W}_x)_{j,k}(x-x_j)+(\boldsymbol{W}_y)_{j,k}(y-y_k),\quad(x,y)\in C_{j,k},\tag{2.14}$$

which results in

$$\begin{aligned} \boldsymbol{W}^{\mathrm{E}}_{j,k} &= \boldsymbol{W}_{j,k} + (\boldsymbol{W}_x)_{j,k}\frac{\Delta x}{2}, \quad \boldsymbol{W}^{\mathrm{W}}_{j,k} = \boldsymbol{W}_{j,k} - (\boldsymbol{W}_x)_{j,k}\frac{\Delta x}{2}, \\ \boldsymbol{W}^{\mathrm{N}}_{j,k} &= \boldsymbol{W}_{j,k} + (\boldsymbol{W}_y)_{j,k}\frac{\Delta y}{2}, \quad \boldsymbol{W}^{\mathrm{S}}_{j,k} = \boldsymbol{W}_{j,k} - (\boldsymbol{W}_y)_{j,k}\frac{\Delta y}{2}. \end{aligned} \tag{2.15}$$

In order for (2.14) to be second-order accurate, the slopes $(\boldsymbol{W}_x)_{j,k}$ and $(\boldsymbol{W}_y)_{j,k}$ have to be at least first-order approximations of $\boldsymbol{W}_x(x_j,y_k)$ and $\boldsymbol{W}_y(x_j,y_k)$, respectively. The nonoscillatory nature of the piecewise linear reconstruction (2.14) is typically ensured with the help of a nonlinear limiter. To all of the components of $\boldsymbol{W}$, we compute the slopes (except for $((b_1)_x)_{j,k}$ and $((b_2)_y)_{j,k}$) using the generalized minmod limiter (see, e.g., [43, 48, 57]):

$$\begin{aligned} (W^{(i)}_x)_{j,k} &= \mathrm{minmod}\left(\theta\frac{W^{(i)}_{j,k}-W^{(i)}_{j-1,k}}{\Delta x}, \frac{W^{(i)}_{j+1,k}-W^{(i)}_{j-1,k}}{2\Delta x}, \right. \\ &\qquad \left. \theta\frac{W^{(i)}_{j+1,k}-W^{(i)}_{j,k}}{\Delta x}\right), \quad i\neq 5, \\ (W^{(i)}_y)_{j,k} &= \mathrm{minmod}\left(\theta\frac{W^{(i)}_{j,k}-W^{(i)}_{j,k-1}}{\Delta y}, \frac{W^{(i)}_{j,k+1}-W^{(i)}_{j,k-1}}{2\Delta y}, \right. \\ &\qquad \left. \theta\frac{W^{(i)}_{j,k+1}-W^{(i)}_{j,k}}{\Delta y}\right), \quad i\neq 6, \end{aligned} \tag{2.16}$$

where the minmod function is defined by

$$\mathrm{minmod}(a_1,a_2,\ldots) = \begin{cases} \min(a_1,a_2,\ldots) & \text{if } a_i>0\ \forall i, \\ \max(a_1,a_2,\ldots) & \text{if } a_i<0\ \forall i, \\ 0 & \text{otherwise.} \end{cases} \tag{2.17}$$

The slopes $((b_1)_x)_{j,k}$ and $((b_2)_y)_{j,k}$, however, should not be computed using the generalized minmod limiter or any other conventional limiter as our goal is to enforce local divergence-free condition (2.3), which at the discrete level reads as $((b_1)_x)_{j,k} + ((b_2)_y)_{j,k} \equiv 0$ for all j,k. This goal can be achieved if we set

$$((b_1)_x)_{j,k} = \overline{A}_{j,k} \quad \text{and} \quad ((b_2)_y)_{j,k} = \overline{B}_{j,k}, \tag{2.18}$$

since

$$\overline{A}_{j,k} + \overline{B}_{j,k} = 0 \tag{2.19}$$

is true for all j,k, provided (2.19) is satisfied at time $t=0$; see Theorem 2.2 in section 2.2.4.

While the use of (2.18) guarantees the local discrete divergence-free condition, the resulting reconstruction of b_1 and b_2 may be oscillatory in the x- and y-directions, respectively. As we have observed in several numerical experiments, this often leads to an oscillatory numerical solution. We, therefore, adjust the slopes in (2.18) by scaling them as follows.

We begin by introducing the auxiliary slopes $(\widehat{(b_1)}_x)_{j,k}$ and $(\widehat{(b_2)}_y)_{j,k}$, which are computed using the aforementioned generalized minmod reconstruction. The reconstructions of b_1 and b_2 can then be made both nonoscillatory and locally divergence-free by replacing (2.18) with

$$((b_1)_x)_{j,k} = \sigma_{j,k}\,\overline{A}_{j,k}, \quad ((b_2)_y)_{j,k} = \sigma_{j,k}\,\overline{B}_{j,k}, \tag{2.20}$$

where

$$\sigma_{j,k}=\min\left\{1,\sigma^x_{j,k},\sigma^y_{j,k}\right\} \tag{2.21}$$

and the scaling factors $\sigma^x_{j,k}$ and $\sigma^y_{j,k}$ are computed by

$$\sigma^x_{j,k}:=\begin{cases}\min\left\{1,\dfrac{(\widehat{(b_1)}_x)_{j,k}}{\overline{A}_{j,k}}\right\} & \text{if } (\widehat{(b_1)}_x)_{j,k}\,\overline{A}_{j,k}>0,\\ 0 & \text{otherwise}\end{cases} \tag{2.22}$$

and

$$\sigma^y_{j,k}:=\begin{cases}\min\left\{1,\dfrac{(\widehat{(b_2)}_y)_{j,k}}{\overline{B}_{j,k}}\right\} & \text{if } (\widehat{(b_2)}_y)_{j,k}\,\overline{B}_{j,k}>0,\\ 0 & \text{otherwise.}\end{cases} \tag{2.23}$$

Finally, equipped with (2.15), we use the EOS (2.2) to compute the cell interface point values $\mathcal{E}^{\mathrm{E,\ W,\ N,\ S}}_{j,k}$ as follows:

$$\begin{aligned}\mathcal{E}^{\ell}_{j,k}=&\frac{p^{\ell}_{j,k}}{\gamma-1}+\frac{1}{2}\rho^{\ell}_{j,k}\left[(u^{\ell}_{j,k})^2+(v^{\ell}_{j,k})^2+(w^{\ell}_{j,k})^2\right]\\&+\frac{1}{2}\left[\left((b_1)^{\ell}_{j,k}\right)^2+\left((b_2)^{\ell}_{j,k}\right)^2+\left((b_3)^{\ell}_{j,k}\right)^2\right],\quad \ell\in\{\mathrm{E},\mathrm{W},\mathrm{N},\mathrm{S}\}.\end{aligned} \tag{2.24}$$

Remark 2.1. We note that we have reconstructed the primitive variables u, v, w, and p rather than the conservative variables ρu, ρv, ρw, and $\mathcal{E}$ since our numerical experiments clearly indicate that the resulting scheme, which is based on the reconstruction of the primitive variables, is less oscillatory and produces no negative pressure values.

It is important to point out that the ninth and tenth components of the fluxes $\boldsymbol{F}(\boldsymbol{U}^{\mathrm{E(W)}}_{j,k})$ and $\boldsymbol{G}(\boldsymbol{U}^{\mathrm{N(S)}}_{j,k})$ depend not only on the corresponding point values of u, v, A, B, b_1, and b_2, but also on the point values of the derivatives $(u_y)^{\mathrm{E(W)}}_{j,k}$ and $(v_x)^{\mathrm{N(S)}}_{j,k}$. We compute these values using first-order approximation, namely, we set

$$(u_y)^{\mathrm{E}}_{j,k}=(u_y)_{j,k},\quad (u_y)^{\mathrm{W}}_{j,k}=(u_y)_{j,k},\quad (v_x)^{\mathrm{N}}_{j,k}=(v_x)_{j,k},\quad (v_x)^{\mathrm{S}}_{j,k}=(v_x)_{j,k},$$

where the slopes $(u_y)_{j,k}$ and $(v_x)_{j,k}$ are computed by (2.16). Notice that even though this will result in the first-order approximation of the auxiliary variables A and B, the other components of $\boldsymbol{U}$ will still be computed with the second order, and thus the second-order accuracy of the resulting scheme will not be affected.

2.2.2. One-sided speeds of propagation. Equipped with the reconstructed point values (2.15) and (2.24), we now proceed with the computation of the one-sided local speeds of propagation $s^{\pm}_{j+\frac{1}{2},k}$ and $s^{\pm}_{j,k+\frac{1}{2}}$ seen in (2.11) and (2.12). We stress that when the PCCU schemes are applied to general nonconservative systems of type (2.6), the x- and y-directional speeds would typically be estimated using the largest and smallest eigenvalues of the matrices $\frac{\partial \boldsymbol{F}}{\partial \boldsymbol{U}}(\boldsymbol{U})-Q(\boldsymbol{U})$ and $\frac{\partial \boldsymbol{G}}{\partial \boldsymbol{U}}(\boldsymbol{U})-R(\boldsymbol{U})$, respectively. However, it is known (see, e.g., [20]) that in the context of the ideal MHD system (2.6)–(2.10), the estimates, which are solely based on the eigenvalues mentioned above, may be inaccurate and using them may lead to severe instabilities.

We therefore follow [64], where the propagation speeds were slightly overestimated to ensure the positivity of both the computed density and pressure, and estimate the right- and left-sided local speeds in the x-direction by

$$\begin{aligned}
s^+_{j+\frac12,k} &= \max\Big\{\max\big\{u^{\rm E}_{j,k}, u^{\rm Roe}_{j+\frac12,k}\big\} + c^{\rm E}_{j,k} + \beta^x_{j+\frac12,k},\\
&\qquad \max\big\{u^{\rm W}_{j+1,k}, u^{\rm Roe}_{j+\frac12,k}\big\} + c^{\rm W}_{j+1,k} + \beta^x_{j+\frac12,k}, 0\Big\},\\
s^-_{j+\frac12,k} &= \min\Big\{\min\big\{u^{\rm E}_{j,k}, u^{\rm Roe}_{j+\frac12,k}\big\} - c^{\rm E}_{j,k} - \beta^x_{j+\frac12,k},\\
&\qquad \min\big\{u^{\rm W}_{j+1,k}, u^{\rm Roe}_{j+\frac12,k}\big\} - c^{\rm W}_{j+1,k} - \beta^x_{j+\frac12,k}, 0\Big\},
\end{aligned}$$

where

$$u^{\rm Roe}_{j+\frac12,k} := \frac{u^{\rm E}_{j,k}\sqrt{\rho^{\rm E}_{j,k}} + u^{\rm W}_{j+1,k}\sqrt{\rho^{\rm W}_{j+1,k}}}{\sqrt{\rho^{\rm E}_{j,k}} + \sqrt{\rho^{\rm W}_{j+1,k}}}, \quad \beta^x_{j+\frac12,k} := \frac{\left|\boldsymbol{b}^{\rm E}_{j,k} - \boldsymbol{b}^{\rm W}_{j+1,k}\right|}{\sqrt{\rho^{\rm E}_{j,k}} + \sqrt{\rho^{\rm W}_{j+1,k}}},$$

and $c^{\rm E(W)}_{j,k}$ are the fast magnetoacoustic wave speeds computed using

$$\begin{aligned}
\Big(c^{\rm E(W)}_{j,k}\Big)^2 = \frac{1}{2\rho^{\rm E(W)}_{j,k}}\Bigg[&\gamma p^{\rm E(W)}_{j,k} + \left|\boldsymbol{b}^{\rm E(W)}_{j,k}\right|^2\\
&+ \sqrt{\left(\gamma p^{\rm E(W)}_{j,k} + \left|\boldsymbol{b}^{\rm E(W)}_{j,k}\right|^2\right)^2 - 4\gamma p^{\rm E(W)}_{j,k}\Big((b_1)^{\rm E(W)}_{j,k}\Big)^2}\Bigg].
\end{aligned}$$

Similarly, we estimate the corresponding y-directional speeds by

$$\begin{aligned}
s^+_{j,k+\frac12} &= \max\Big\{\max\big\{v^{\rm N}_{j,k}, v^{\rm Roe}_{j,k+\frac12}\big\} + c^{\rm N}_{j,k} + \beta^y_{j,k+\frac12},\\
&\qquad \max\big\{v^{\rm S}_{j,k+1}, v^{\rm Roe}_{j,k+\frac12}\big\} + c^{\rm S}_{j,k+1} + \beta^y_{j,k+\frac12}, 0\Big\},\\
s^-_{j,k+\frac12} &= \min\Big\{\min\big\{v^{\rm N}_{j,k}, v^{\rm Roe}_{j,k+\frac12}\big\} - c^{\rm N}_{j,k} - \beta^y_{j,k+\frac12},\\
&\qquad \min\big\{v^{\rm S}_{j,k+1}, v^{\rm Roe}_{j,k+\frac12}\big\} - c^{\rm S}_{j,k+1} - \beta^y_{j,k+\frac12}, 0\Big\},
\end{aligned}$$

where

$$\begin{aligned}
&v^{\rm Roe}_{j,k+\frac12} := \frac{v^{\rm N}_{j,k}\sqrt{\rho^{\rm N}_{j,k}} + v^{\rm S}_{j,k+1}\sqrt{\rho^{\rm S}_{j,k+1}}}{\sqrt{\rho^{\rm N}_{j,k}} + \sqrt{\rho^{\rm S}_{j,k+1}}}, \quad \beta^y_{j,k+\frac12} := \frac{\left|\boldsymbol{b}^{\rm N}_{j,k} - \boldsymbol{b}^{\rm S}_{j,k+1}\right|}{\sqrt{\rho^{\rm N}_{j,k}} + \sqrt{\rho^{\rm S}_{j,k+1}}},\\
&\Big(c^{\rm N(S)}_{j,k}\Big)^2 = \frac{1}{2\rho^{\rm N(S)}_{j,k}}\Bigg[\gamma p^{\rm N(S)}_{j,k} + \left|\boldsymbol{b}^{\rm N(S)}_{j,k}\right|^2\\
&\qquad + \sqrt{\left(\gamma p^{\rm N(S)}_{j,k} + \left|\boldsymbol{b}^{\rm N(S)}_{j,k}\right|^2\right)^2 - 4\gamma p^{\rm N(S)}_{j,k}\Big((b_2)^{\rm N(S)}_{j,k}\Big)^2}\Bigg].
\end{aligned}$$

2.2.3. Discretization of the nonconservative products. In this section, we provide the computation of the nonconservative product terms in (2.11).

Following [8] (see also [11]), we obtain nonconservative terms in the x-direction, $\boldsymbol{Q}_{j,k}$ and $\boldsymbol{Q}_{\boldsymbol{\Psi},j+\frac12,k}$, as follows. First, in order to compute the term $\boldsymbol{Q}_{j,k}$, we take a

global (in space) interpolant $\boldsymbol{U}(\widetilde{\boldsymbol{W}}(x,y))$, where $\widetilde{\boldsymbol{W}}$ is given by (2.14), and evaluate the integral in

$$\boldsymbol{Q}_{j,k}=\int_{x_{j-\frac12}}^{x_{j+\frac12}} Q\big(\boldsymbol{U}\big(\widetilde{\boldsymbol{W}}(x,y_k)\big)\big)\boldsymbol{U}(\widetilde{\boldsymbol{W}}(x,y_k))_x\,\mathrm{d}x,$$

where $Q(\boldsymbol{U})$ is defined as in (2.9), exactly. This results in the following expressions for the ten components of the vector $\boldsymbol{Q}_{j,k}$:

$$\begin{aligned}
&Q^{(1)}_{j,k}=Q^{(9)}_{j,k}=Q^{(10)}_{j,k}=0,\\
&Q^{(i)}_{j,k}=-\int_{x_{j-\frac12}}^{x_{j+\frac12}}\widetilde{b_{i-1}}(x,y_k)((b_1)_x)_{j,k}\,\mathrm{d}x=-(\overline{b_{i-1}})_{j,k}\sigma_{j,k}\,\overline{A}_{j,k}\Delta x,\quad i=2,3,4,\\
&\Big(Q^{(5)}_{j,k},Q^{(6)}_{j,k},Q^{(7)}_{j,k}\Big)^{\top}=-\int_{x_{j-\frac12}}^{x_{j+\frac12}}\widetilde{\boldsymbol{u}}(x,y_k)((b_1)_x)_{j,k}\,\mathrm{d}x=-\boldsymbol{u}_{j,k}\sigma_{j,k}\,\overline{A}_{j,k}\Delta x,\\
&Q^{(8)}_{j,k}=-\int_{x_{j-\frac12}}^{x_{j+\frac12}}\widetilde{\boldsymbol{u}}(x,y_k)\cdot\widetilde{\boldsymbol{b}}(x,y_k)((b_1)_x)_{j,k}\,\mathrm{d}x=-\Big[\Big(\boldsymbol{u}_{j,k}\cdot\boldsymbol{b}_{j,k}\\
&\qquad+\frac{(\Delta x)^2}{12}\left\{(u_x)_{j,k}\sigma_{j,k}\,\overline{A}_{j,k}+(v_x)_{j,k}((b_2)_x)_{j,k}+(w_x)_{j,k}((b_3)_x)_{j,k}\right\}\Big)\Big]\sigma_{j,k}\,\overline{A}_{j,k}\Delta x,
\end{aligned}$$

where we have used the slopes $((b_1)_x)_{j,k}$ given by (2.20)–(2.23), while the other slopes are computed as in (2.16)–(2.17).

Next, the terms $\boldsymbol{Q}_{\boldsymbol{\Psi},j+\frac12,k}$ are computed by the exact integration of

$$\boldsymbol{Q}_{\boldsymbol{\Psi},j+\frac12,k}=\int_0^1 Q\big(\boldsymbol{U}\big(\boldsymbol{\Psi}_{j+\frac12,k}(s)\big)\big)\boldsymbol{\Psi}'_{j+\frac12,k}(s)\,\mathrm{d}s,$$

where $\boldsymbol{\Psi}_{j+\frac12,k}(s)$ is a linear path connecting the states $\boldsymbol{W}^{\mathrm{E}}_{j,k}$ and $\boldsymbol{W}^{\mathrm{W}}_{j+1,k}$:

$$\boldsymbol{\Psi}_{j+\frac12,k}(s)=\boldsymbol{W}^{\mathrm{E}}_{j,k}+s\Big(\boldsymbol{W}^{\mathrm{W}}_{j+1,k}-\boldsymbol{W}^{\mathrm{E}}_{j,k}\Big).$$

This results in

$$\begin{aligned}
&Q^{(1)}_{\boldsymbol{\Psi},j+\frac12,k}=Q^{(9)}_{\boldsymbol{\Psi},j+\frac12,k}=Q^{(10)}_{\boldsymbol{\Psi},j+\frac12,k}=0,\\
&Q^{(i)}_{\boldsymbol{\Psi},j+\frac12,k}=-\int_0^1\left\{(b_{i-1})^{\mathrm{E}}_{j,k}+s\big((b_{i-1})^{\mathrm{W}}_{j+1,k}-(b_{i-1})^{\mathrm{E}}_{j,k}\big)\right\}[b_1]_{j+\frac12,k}\,\mathrm{d}s\\
&\qquad=-\frac12\left((b_{i-1})^{\mathrm{E}}_{j,k}+(b_{i-1})^{\mathrm{W}}_{j+1,k}\right)[b_1]_{j+\frac12,k},\quad i=2,3,4,\\
&\Big(Q^{(5)}_{\boldsymbol{\Psi},j+\frac12,k},Q^{(6)}_{\boldsymbol{\Psi},j+\frac12,k},Q^{(7)}_{\boldsymbol{\Psi},j+\frac12,k}\Big)^{\top}=-\int_0^1\left\{\boldsymbol{u}^{\mathrm{E}}_{j,k}+s\big(\boldsymbol{u}^{\mathrm{W}}_{j+1,k}-\boldsymbol{u}^{\mathrm{E}}_{j,k}\big)\right\}[b_1]_{j+\frac12,k}\,\mathrm{d}s\\
&\qquad\qquad=-\frac12\left(\boldsymbol{u}^{\mathrm{E}}_{j,k}+\boldsymbol{u}^{\mathrm{W}}_{j+1,k}\right)[b_1]_{j+\frac12,k},\\
&Q^{(8)}_{\boldsymbol{\Psi},j+\frac12,k}=-\int_0^1\left\{\boldsymbol{u}^{\mathrm{E}}_{j,k}+s\big(\boldsymbol{u}^{\mathrm{W}}_{j+1,k}-\boldsymbol{u}^{\mathrm{E}}_{j,k}\big)\right\}\cdot\left\{\boldsymbol{b}^{\mathrm{E}}_{j,k}+s\Big(\boldsymbol{b}^{\mathrm{W}}_{j+1,k}-\boldsymbol{b}^{\mathrm{E}}_{j,k}\Big)\right\}[b_1]_{j+\frac12,k}\,\mathrm{d}s\\
&\qquad=-\frac16\Big(2\boldsymbol{u}^{\mathrm{E}}_{j,k}\cdot\boldsymbol{b}^{\mathrm{E}}_{j,k}+\boldsymbol{u}^{\mathrm{E}}_{j,k}\cdot\boldsymbol{b}^{\mathrm{W}}_{j+1,k}+\boldsymbol{u}^{\mathrm{W}}_{j+1,k}\cdot\boldsymbol{b}^{\mathrm{E}}_{j,k}+2\boldsymbol{u}^{\mathrm{W}}_{j+1,k}\cdot\boldsymbol{b}^{\mathrm{W}}_{j+1,k}\Big)[b_1]_{j+\frac12,k},
\end{aligned}$$

where $[b_1]_{j+\frac12,k}:=(b_1)^{\mathrm{W}}_{j+1,k}-(b_1)^{\mathrm{E}}_{j,k}$.

Similarly, we obtain the following formulae for the nonconservative terms in the y-direction, $\boldsymbol{R}_{j,k}$ and $\boldsymbol{R}_{\boldsymbol{\Psi},j,k+\frac{1}{2}}$:

$$
\begin{aligned}
&R^{(1)}_{j,k}=R^{(9)}_{j,k}=R^{(10)}_{j,k}=0,\quad R^{(i)}_{j,k}=-(\overline{b_{i-1}})_{j,k}\sigma_{j,k}\,\overline{B}_{j,k}\Delta y,\quad i=2,3,4,\\
&\big(R^{(5)}_{j,k},R^{(6)}_{j,k},R^{(7)}_{j,k}\big)^\top=-\boldsymbol{u}_{j,k}\sigma_{j,k}\,\overline{B}_{j,k}\Delta y,\\
&R^{(8)}_{j,k}=-\Big[\Big(\boldsymbol{u}_{j,k}\cdot\boldsymbol{b}_{j,k}+\frac{(\Delta y)^2}{12}\left\{(u_y)_{j,k}((b_1)_y)_{j,k}+(v_y)_{j,k}\sigma_{j,k}\,\overline{B}_{j,k}\right.\\
&\qquad\qquad\left.+(w_y)_{j,k}((b_3)_y)_{j,k}\right\}\Big)\Big]\sigma_{j,k}\,\overline{B}_{j,k}\Delta y,
\end{aligned}
$$

where we have used the slopes $((b_2)_y)_{j,k}$ given by (2.20)–(2.23), while the other slopes are computed as in (2.16)–(2.17), and

$$
\begin{aligned}
&R^{(1)}_{\boldsymbol{\Psi},j,k+\frac{1}{2}}=R^{(9)}_{\boldsymbol{\Psi},j,k+\frac{1}{2}}=R^{(10)}_{\boldsymbol{\Psi},j,k+\frac{1}{2}}=0,\\
&R^{(i)}_{\boldsymbol{\Psi},j,k+\frac{1}{2}}=-\frac{1}{2}\left((b_{i-1})^{\rm N}_{j,k}+(b_{i-1})^{\rm S}_{j,k+1}\right)[b_2]_{j,k+\frac{1}{2}},\quad i=2,3,4,\\
&\big(R^{(5)}_{\boldsymbol{\Psi},j,k+\frac{1}{2}},R^{(6)}_{\boldsymbol{\Psi},j,k+\frac{1}{2}},R^{(7)}_{\boldsymbol{\Psi},j,k+\frac{1}{2}}\big)^\top=-\frac{1}{2}\left(\boldsymbol{u}^{\rm N}_{j,k}+\boldsymbol{u}^{\rm S}_{j,k+1}\right)[b_2]_{j,k+\frac{1}{2}},\\
&R^{(8)}_{\boldsymbol{\Psi},j,k+\frac{1}{2}}=-\frac{1}{6}\Big(2\boldsymbol{u}^{\rm N}_{j,k}\cdot\boldsymbol{b}^{\rm N}_{j,k}+\boldsymbol{u}^{\rm N}_{j,k}\cdot\boldsymbol{b}^{\rm S}_{j,k+1}+\boldsymbol{u}^{\rm S}_{j,k+1}\cdot\boldsymbol{b}^{\rm N}_{j,k}+2\boldsymbol{u}^{\rm S}_{j,k+1}\cdot\boldsymbol{b}^{\rm S}_{j,k+1}\Big)[b_2]_{j,k+\frac{1}{2}},
\end{aligned}
$$

where $[b_2]_{j,k+\frac{1}{2}}:=((b_2)^{\rm S}_{j,k+1}-(b_2)^{\rm N}_{j,k})$.

2.2.4. Local divergence-free property. We now prove the local divergence-free property of the proposed PCCU scheme.

THEOREM 2.2. *For the PCCU scheme* (2.11)–(2.12) *with the reconstruction described in section* 2.2.1*, the local divergence-free condition*

$$
\big((b_1)_x\big)_{j,k}+\big((b_2)_y\big)_{j,k}=0 \tag{2.25}
$$

holds for all j,k and at all times, provided it is satisfied initially.

Proof. First, we note that according to (2.20),

$$
\big((b_1)_x\big)_{j,k}+\big((b_2)_y\big)_{j,k}=\sigma_{j,k}\left(\overline{A}_{j,k}+\overline{B}_{j,k}\right).
$$

Therefore, in order to prove (2.25), it is sufficient to show that $\overline{A}_{j,k}+\overline{B}_{j,k}=0$ for all j,k and for all times assuming that it is satisfied at the initial time $t=0$.

We then observe that the quantities $\overline{A}_{j,k}$ and $\overline{B}_{j,k}$ are the ninth and tenth components of $\overline{\boldsymbol{U}}_{j,k}$, and thus they are evolved in time by numerically integrating the ninth and tenth components of (2.11)–(2.12). Adding these components in (2.11) results in

$$
\begin{aligned}
\frac{\rm d}{{\rm d}t}\left(\overline{A}_{j,k}+\overline{B}_{j,k}\right)=&-\frac{1}{\Delta x}\left[\mathcal{F}^{(9)}_{j+\frac{1}{2},k}-\mathcal{F}^{(9)}_{j-\frac{1}{2},k}+\mathcal{F}^{(10)}_{j+\frac{1}{2},k}-\mathcal{F}^{(10)}_{j-\frac{1}{2},k}\right]\\
&-\frac{1}{\Delta y}\left[\mathcal{G}^{(9)}_{j,k+\frac{1}{2}}-\mathcal{G}^{(9)}_{j,k-\frac{1}{2}}+\mathcal{G}^{(10)}_{j,k+\frac{1}{2}}-\mathcal{G}^{(10)}_{j,k-\frac{1}{2}}\right].
\end{aligned} \tag{2.26}
$$

In order to complete the proof, it is sufficient to show that the RHS of (2.26) vanishes as long as $\overline{A}_{j,k}+\overline{B}_{j,k}=0$ for all j,k. To this end, we use (2.12) to evaluate

$$
\begin{aligned}
&\mathcal{F}^{(9)}_{j+\frac12,k}-\mathcal{F}^{(9)}_{j-\frac12,k}+\mathcal{F}^{(10)}_{j+\frac12,k}-\mathcal{F}^{(10)}_{j-\frac12,k}\\
&\quad=\frac{s^+_{j+\frac12,k}\Big[u^{\rm E}_{j,k}\Big(A^{\rm E}_{j,k}+B^{\rm E}_{j,k}\Big)\Big]-s^-_{j+\frac12,k}\Big[u^{\rm W}_{j+1,k}\Big(A^{\rm W}_{j+1,k}+B^{\rm W}_{j+1,k}\Big)\Big]}{s^+_{j+\frac12,k}-s^-_{j+\frac12,k}}\\
&\qquad+\frac{s^+_{j+\frac12,k}s^-_{j+\frac12,k}}{s^+_{j+\frac12,k}-s^-_{j+\frac12,k}}\Big[\big(A^{\rm W}_{j+1,k}+B^{\rm W}_{j+1,k}\big)-\big(A^{\rm E}_{j,k}+B^{\rm E}_{j,k}\big)\Big]\\
&\quad\overset{(2.15)}{=}\frac{s^+_{j+\frac12,k}}{s^+_{j+\frac12,k}-s^-_{j+\frac12,k}}\Big[u^{\rm E}_{j,k}\Big(\overline{A}_{j,k}+\frac{\Delta x}{2}(A_x)_{j,k}+\overline{B}_{j,k}+\frac{\Delta x}{2}(B_x)_{j,k}\Big)\Big]\\
&\qquad-\frac{s^-_{j+\frac12,k}}{s^+_{j+\frac12,k}-s^-_{j+\frac12,k}}\Big[u^{\rm W}_{j+1,k}\Big(\overline{A}_{j+1,k}-\frac{\Delta x}{2}(A_x)_{j+1,k}+\overline{B}_{j+1,k}-\frac{\Delta x}{2}(B_x)_{j+1,k}\Big)\Big]\\
&\qquad+\frac{s^+_{j+\frac12,k}s^-_{j+\frac12,k}}{s^+_{j+\frac12,k}-s^-_{j+\frac12,k}}\Big[\overline{A}_{j+1,k}-\frac{\Delta x}{2}(A_x)_{j+1,k}+\overline{B}_{j+1,k}-\frac{\Delta x}{2}(B_x)_{j+1,k}\Big]\\
&\qquad-\frac{s^+_{j+\frac12,k}s^-_{j+\frac12,k}}{s^+_{j+\frac12,k}-s^-_{j+\frac12,k}}\Big[\overline{A}_{j,k}+\frac{\Delta x}{2}(A_x)_{j,k}+\overline{B}_{j,k}+\frac{\Delta x}{2}(B_x)_{j,k}\Big]\\
&\quad=\frac{\Delta x}{2}\Bigg\{\frac{s^+_{j+\frac12,k}\Big[u^{\rm E}_{j,k}\big((A_x)_{j,k}+(B_x)_{j,k}\big)\Big]+s^-_{j+\frac12,k}\Big[u^{\rm W}_{j+1,k}\big((A_x)_{j+1,k}+(B_x)_{j+1,k}\big)\Big]}{s^+_{j+\frac12,k}-s^-_{j+\frac12,k}}\\
&\qquad-\frac{s^+_{j+\frac12,k}s^-_{j+\frac12,k}}{s^+_{j+\frac12,k}-s^-_{j+\frac12,k}}\Big[(A_x)_{j+1,k}+(B_x)_{j+1,k}+(A_x)_{j,k}+(B_x)_{j,k}\Big]\Bigg\},
\end{aligned}
$$

where the last equality is obtained using $\overline{A}_{j,k}+\overline{B}_{j,k}=\overline{A}_{j+1,k}+\overline{B}_{j+1,k}=0$.

It is now clear that $\mathcal{F}^{(9)}_{j+\frac12,k}-\mathcal{F}^{(9)}_{j-\frac12,k}+\mathcal{F}^{(10)}_{j+\frac12,k}-\mathcal{F}^{(10)}_{j-\frac12,k}$ will be identically zero as long as

$$
(A_x)_{j,k}+(B_x)_{j,k}=0 \tag{2.27}
$$

for all j,k. Indeed, (2.27) is true since $\overline{A}_{j,k}=-\overline{B}_{j,k}$ for all j,k and both the slopes $(A_x)_{j,k}$ and $(B_x)_{j,k}$ are computed using the same limiter (2.16).

Similarly, one can show that $\mathcal{G}^{(9)}_{j,k+\frac12}-\mathcal{G}^{(9)}_{j,k-\frac12}+\mathcal{G}^{(10)}_{j,k+\frac12}-\mathcal{G}^{(10)}_{j,k-\frac12}\equiv0$, so that the RHS of (2.26) vanishes, and thus the proof of the theorem is complete. ∎

2.3. Numerical examples. In this section, we demonstrate the performance of the proposed PCCU scheme in several numerical experiments conducted for the augmented 2-D ideal MHD system (2.6)-(2.10), (2.2). In all of the examples in this section, we follow the CFL condition in (2.13) and take the CFL number $\eta=0.25$ and the minmod parameter $\theta=1.3$.

Example 1*—Brio–Wu shock-tube problem.* In the first example, we consider the one-dimensional (1-D) Riemann problem known as the Brio–Wu shock-tube problem, originally presented in [7]. This problem is the standard test for capturing compound waves that emerge as solutions of the ideal MHD system. We take the following initial data, which depend on x only:

$$
(\rho,u,v,w,b_1,b_2,b_3,p)\Big|_{(x,y,0)}=\begin{cases}(1,0,0,0,0.75,1,0,1), & x<0,\\ (0.125,0,0,0,0.75,-1,0,0.1) & \text{otherwise.}\end{cases}
$$

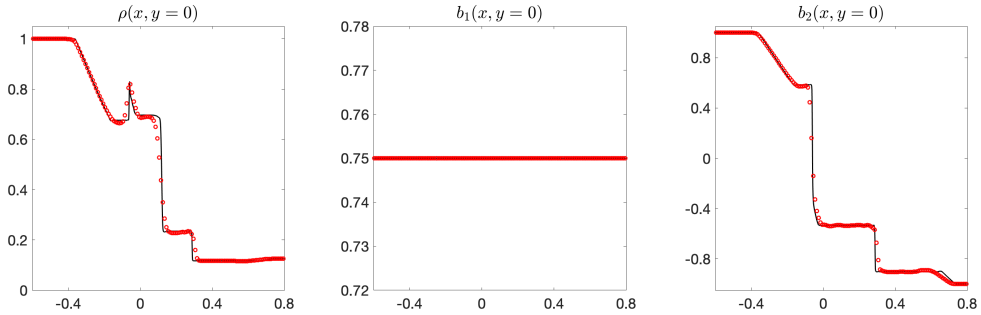

FIG. 2.1. *Example* 1: ρ, b_1, *and* b_2 *computed by the PCCU scheme on* 200×2 *(red circles) and* 1600×16 *(solid black line) uniform meshes.*

We set the free boundary conditions on all sides of the computational domain $[-1,1]\times[-0.01,0.01]$. The specific heat ratio is $\gamma=2$ in this example.

In Figure 2.1, we plot the $y=0$ cross-section of the density ρ, x-magnetic field b_1, and y-magnetic field b_2 computed on 200×2 and 1600×16 uniform meshes at time $t=0.2$. As one can see, the solution to this 1-D Riemann problem consists of several nonsmooth structures, such as rarefaction waves, shocks traveling at various speeds, a contact discontinuity, and a compound shock wave. The proposed PCCU scheme captures all of these complicated structures well, even on a coarser mesh, and the obtained results strongly agree with those reported in [19, 23, 40, 42, 45].

Example 2*—circularly polarized Alfvén wave.* In the second example, taken from [58], we consider the time evolution of a circularly polarized Alfvén wave that travels at a constant speed at an angle of $\alpha=\pi/6$ with respect to the x-axis. The initial conditions are

$$\begin{aligned}&\rho(x,y,0)\equiv 1, \quad u(x,y,0)=v_\parallel\cos\alpha+v_\perp\sin\alpha, \quad v(x,y,0)=v_\parallel\sin\alpha-v_\perp\cos\alpha,\\ &p(x,y,0)\equiv 0.1, \quad b_1(x,y,0)=b_\parallel\cos\alpha+b_\perp\sin\alpha, \quad b_2(x,y,0)=b_\parallel\sin\alpha-b_\perp\cos\alpha,\end{aligned}$$

$$w(x,y,0)=b_3(x,y,0)=0.1\cos\big[2\pi(x\cos\alpha+y\sin\alpha)\big],$$

where

$$v_\parallel=0, \quad b_\parallel=1, \quad v_\perp=b_\perp=0.1\sin\big[2\pi(x\cos\alpha+y\sin\alpha)\big].$$

We use a specific heat ratio $\gamma=5/3$, take the computational domain $[0,1/\cos\alpha]\times[0,1/\sin\alpha]$, and prescribe the periodic boundary conditions in both the x- and y-directions. It is easy to show that the solution of the resulting initial-boundary value problem is a traveling wave, which returns to its initial position at any integer t.

We compute the solution on an $N\times N$ uniform mesh and compute the L^1-errors when the solution reaches the final time $t=5$. Both the errors and corresponding experimental rates of convergence for u and b_3 are presented in Table 2.1. From this data, one can see that the proposed scheme does indeed achieve the expected second order of accuracy.

Example 3*—Orszag–Tang vortex problem.* In this example, we consider the Orszag–Tang vortex problem, which was introduced in [49] and has been widely used as a benchmark due to the formation and interaction of multiple shocks as the system evolves in time and to the presence of many important features of MHD turbulence; see, e.g., [19, 41, 42, 44, 67]. The initial conditions for this problem read as

TABLE 2.1
Example 2: L^1*-errors for* u *and* b_3 *and the corresponding experimental rates of convergence.*

N	$\|u(x,y,5)-u(x,y,0)\|_1$	Rate	$\|b_3(x,y,5)-b_3(x,y,0)\|_1$	Rate
20	1.96e-02	–	4.24e-02	–
40	4.63e-03	2.08	1.10e-02	1.95
80	1.47e-03	1.65	3.48e-03	1.66
160	3.88e-04	1.92	9.24e-04	1.91
320	9.34e-05	2.06	2.20e-04	2.07

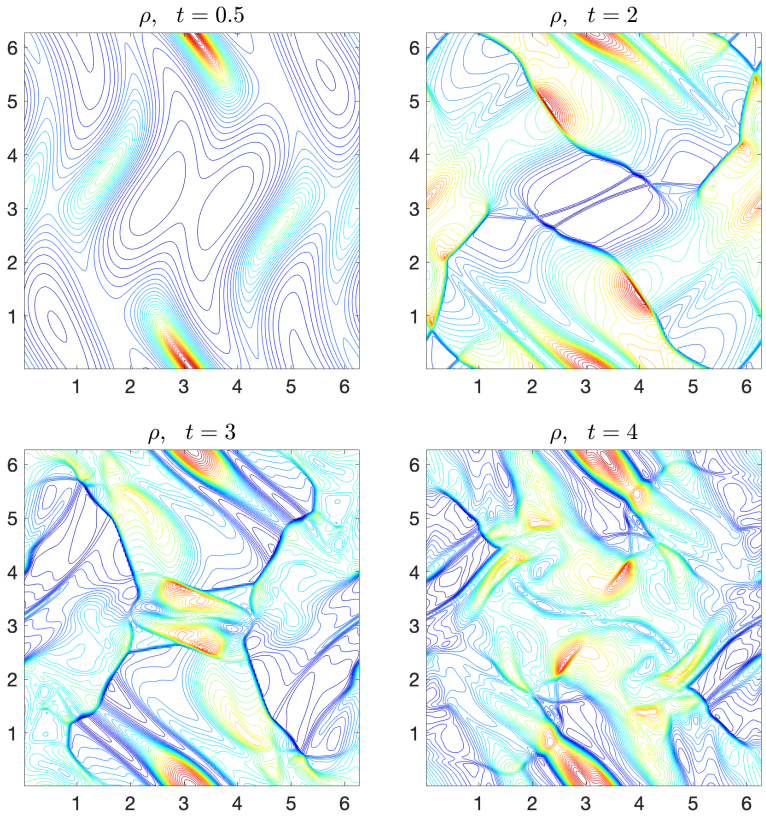

FIG. 2.2. *Example* 3: *Fluid density* ρ *computed by the proposed PCCU scheme at different times.* 40 *equally spaced contours are used in each plot with the ranges* $[2.11, 5.83]$, $[0.63, 6.17]$, $[1.29, 6.12]$, *and* $[1.25, 5.8]$, *respectively.*

$$\rho(x,y,0)\equiv\gamma^2,\quad u(x,y,0)=-\sin y,\quad v(x,y,0)=\sin x,\quad w(x,y,0)\equiv 0,$$
$$b_1(x,y,0)=-\sin y,\quad b_2(x,y,0)=\sin(2x),\quad b_3(x,y,0)\equiv 0,\quad p(x,y,0)\equiv\gamma,$$

where $\gamma=5/3$ is the specific heat ratio. We set the periodic boundary conditions on all sides of the computational domain $[0,2\pi]\times[0,2\pi]$.

The time evolution of the fluid density ρ computed on a uniform 200×200 mesh is shown at times $t=0.5$, 2, 3, and 4 in Figure 2.2. We observe that the numerical solution computed by the proposed PCCU scheme remains stable and is consistent with previous results presented in [41, 42, 44, 67], demonstrating the ability of our scheme to capture both smooth flows and shocks.

Example 4*—rotor problem.* Next, we consider the "second rotor problem" from [5, 58], referred to as the rotor problem in this paper. This commonly used benchmark

problem describes a rapidly rotating disk of dense fluid centered in a background of static fluid. Over time, the disk expands and rotates. The initial conditions are given by

$$(\rho,u,v)\Big|_{(x,y,0)}=\begin{cases}\left(10,\dfrac{0.5-y}{r_0},\dfrac{x-0.5}{r_0}\right), & r<0.1,\\ \left(1+9\lambda,\dfrac{\lambda(0.5-y)}{r},\dfrac{\lambda(x-0.5)}{r}\right), & 0.1\le r\le 0.115,\\ (1,0,0), & r>0.115,\end{cases}$$

$$w(x,y,0)=b_2(x,y,0)=b_3(x,y,0)\equiv 0,\quad b_1(x,y,0)\equiv\frac{2.5}{\sqrt{4\pi}},\quad p(x,y,0)\equiv 0.5,$$

where $r=\sqrt{(x-0.5)^2+(y-0.5)^2}$ and $\lambda=(0.115-r)/0.015$. We take the specific heat ratio $\gamma=5/3$ and use the periodic boundary conditions on all sides of the computational domain $[0,1]\times[0,1]$.

In Figure 2.3, we show the fluid density ρ, pressure p, Mach number $|\boldsymbol{u}|/c_s$ (where $c_s=\sqrt{\gamma p/\rho}$ is the speed of sound), and magnetic pressure $|\boldsymbol{b}|^2/2$ computed on a uniform 200×200 mesh at time $t=0.295$. We note that our results are in good agreement with those reported in, e.g., [42, 44, 58]. In addition, it is emphasized in [5, 44, 58] that, due to rapid changes at the center of the rotation, many numerical methods produce oscillations or negative pressure values. We stress that during numerical simulations, we have not observed any oscillations, and the proposed PCCU scheme has produced no negative values of the computed pressure. The oscillation-free feature is

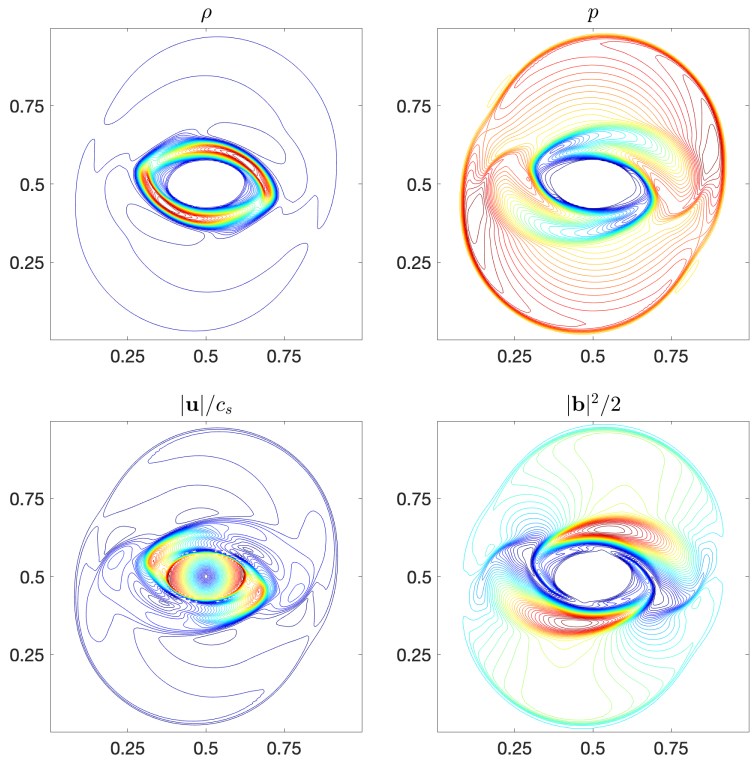

FIG. 2.3. *Example* 4: *Fluid density* ρ, *pressure* p, *Mach number* $|\boldsymbol{u}|/c_s$, *and magnetic pressure* $|\boldsymbol{b}|^2/2$ *computed by the proposed PCCU scheme.* 40 *equally spaced contours are used in each plot with the ranges* $[0.71,8.95]$, $[0.01,0.78]$, $[0,2.9]$, *and* $[0.02,0.65]$, *respectively.*

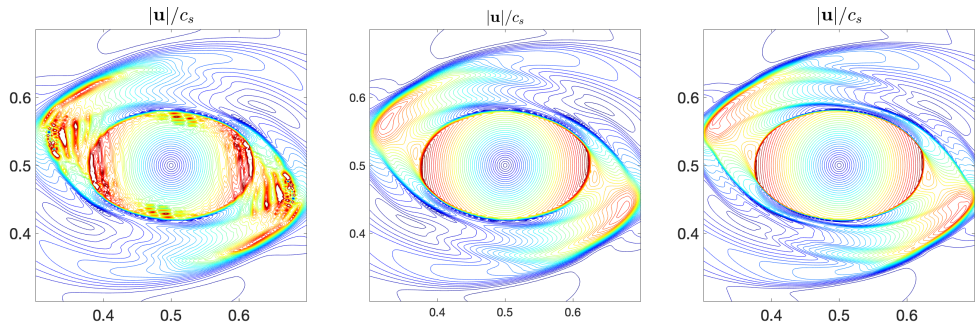

FIG. 2.4. *Example* 4: *Zoom-in of the center of the Mach number plots computed on a* 400×400 *mesh without any divergence-free treatment (left), on a* 400×400 *mesh using the proposed scheme (middle), and on a* 800×800 *mesh using the proposed scheme (right).* 40 *equally spaced contours in the range* $[0, 2.9]$ *are used in each plot.*

further illustrated in Figure 2.4, where we zoom in on the center of the Mach number computed with our proposed scheme (middle and right panels), creating oscillation-free solutions, and the analogous CU scheme (see, e.g., [37]) without any divergence-free treatment (left panel), which returns a solution with clear spurious oscillations.

Example 5—*blast problem.* In this example, we consider the blast problem, first introduced in [5]. This benchmark problem is seen in a number of studies (see, e.g., [41, 42, 44, 67]) and is considered a challenge due to the low gas pressure and strong magnetosonic shocks. Negative pressures are easily produced near the shocks; see [41, 42] and references therein. The initial conditions are

$$(\rho, u, v, w, b_1, b_2, b_3)\Big|_{(x,y,0)} = \left(1, 0, 0, 0, \frac{100}{\sqrt{4\pi}}, 0, 0\right),$$
$$p(x, y, 0) = \begin{cases} 1000, & \sqrt{x^2 + y^2} < 0.1, \\ 0.1 & \text{otherwise.} \end{cases}$$

We take the specific heat ratio $\gamma = 1.4$ and use zero-order extrapolation on the boundaries of the computational domain $[-0.5, 0.5] \times [-0.5, 0.5]$.

The fluid density ρ, pressure p, magnitude of velocity $|\boldsymbol{u}|$, and magnetic pressure $|\boldsymbol{b}|^2/2$ computed by the proposed PCCU scheme on a 200×200 uniform mesh at $t = 0.01$ are depicted in Figure 2.5. Additionally, the numerical experimentation of the proposed method resulted in positive pressure values throughout the entire computational domain, returning a minimum pressure of 0.10. Positive pressure values are also completely maintained when running the blast problem on a refined 400×400 uniform grid (the fine mesh results are not shown here for brevity).

3. Shallow water MHD.

3.1. Governing equations. In this section, we study the modified Godunov–Powell shallow water MHD system, which reads as

$$\begin{aligned}
&h_t + (hu)_x + (hv)_y = 0, \\
&(hu)_t + \left(hu^2 + \frac{g}{2}h^2 - ha^2\right)_x + (huv - hab)_y = -a\left[(ha)_x + (hb)_y\right], \\
&(hv)_t + (huv - hab)_x + \left(hv^2 + \frac{g}{2}h^2 - hb^2\right)_y = -b\left[(ha)_x + (hb)_y\right], \\
&(ha)_t + (hbu - hav)_y = -u\left[(ha)_x + (hb)_y\right], \\
&(hb)_t + (hav - hbu)_x = -v\left[(ha)_x + (hb)_y\right].
\end{aligned} \tag{3.1}$$

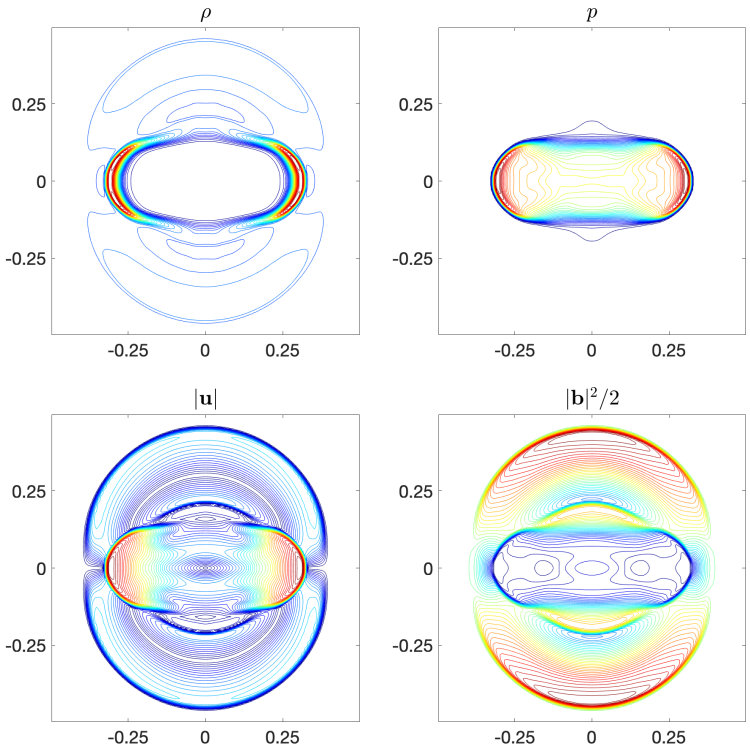

FIG. 2.5. *Example* 5: *Fluid density* ρ, *pressure* p, *velocity magnitude* $|\boldsymbol{u}|$, *and magnetic pressure* $|\boldsymbol{b}|^2/2$ *computed by the proposed PCCU scheme.* 40 *equally spaced contours are used in each plot with the ranges* $[0.22, 4.09]$, $[0.10, 250]$, $[0, 16.77]$, *and* $[215, 588]$, *respectively.*

Here, h is the fluid thickness, u and v represent the x- and y-velocity, $(a, b)^\top$ is the reduced magnetic field, which has units of velocity, and g is the acceleration due to gravity. As in the ideal MHD system considered in section 2, one can easily show that

$$(ha)_x + (hb)_y = 0 \tag{3.2}$$

as long as the field $(ha, hb)^\top$ is initially divergence-free. Therefore, the Godunov–Powell source terms on the RHS of (3.1) are theoretically zero. Still, they are added to the original shallow water MHD system to help enforce the divergence-free constraint (3.2) numerically; see, e.g., [32, 33, 61].

In order to develop a locally divergence-free numerical method for the system (3.1), this divergence constraint (3.2) must be enforced on the discrete level. As in section 2, we achieve this goal by introducing the new variables $A := (ha)_x$ and $B := (hb)_y$, differentiating the induction equation in (3.1) with respect to x and y, and obtaining the following equations for A and B:

$$\begin{aligned} &A_t + \big(uA - hbu_y\big)_x + \big(vA + hav_x\big)_y = 0,\\ &B_t + \big(uB + hbu_y\big)_x + \big(vB - hav_x\big)_y = 0, \end{aligned} \tag{3.3}$$

which are then added to the studied system (3.1).

Prior to introducing the numerical method for the augmented system (3.1), (3.3), we write it in the vector form

$$\boldsymbol{U}_t + \boldsymbol{F}(\boldsymbol{U})_x + \boldsymbol{G}(\boldsymbol{U})_y = Q(\boldsymbol{U})\boldsymbol{U}_x + R(\boldsymbol{U})\boldsymbol{U}_y, \tag{3.4}$$

where $\boldsymbol{U} := (h, hu, hv, ha, hb, A, B)^\top$,

$$\boldsymbol{F}(\boldsymbol{U}) = \Big(hu, hu^2 + \frac{g}{2}gh^2 - ha^2, huv - hab, 0, hbu - hav, uA - hbu_y, uB + hbu_y\Big)^\top,$$

$$\boldsymbol{G}(\boldsymbol{U}) = \Big(hv, huv - hab, hv^2 + \frac{g}{2}h^2 - hb^2, hav - hbu, 0, vA + hav_x, vB - hav_x,\Big)^\top,$$

$$Q(\boldsymbol{U}) = \begin{pmatrix} 0 & 0 & 0 & 0 & 0 & 0 & 0 \\ 0 & 0 & 0 & -a & 0 & 0 & 0 \\ 0 & 0 & 0 & -b & 0 & 0 & 0 \\ 0 & 0 & 0 & -u & 0 & 0 & 0 \\ 0 & 0 & 0 & -v & 0 & 0 & 0 \\ 0 & 0 & 0 & 0 & 0 & 0 & 0 \\ 0 & 0 & 0 & 0 & 0 & 0 & 0 \end{pmatrix}, \quad R(\boldsymbol{U}) = \begin{pmatrix} 0 & 0 & 0 & 0 & 0 & 0 & 0 \\ 0 & 0 & 0 & 0 & -a & 0 & 0 \\ 0 & 0 & 0 & 0 & -b & 0 & 0 \\ 0 & 0 & 0 & 0 & -u & 0 & 0 \\ 0 & 0 & 0 & 0 & -v & 0 & 0 \\ 0 & 0 & 0 & 0 & 0 & 0 & 0 \\ 0 & 0 & 0 & 0 & 0 & 0 & 0 \end{pmatrix}.$$

3.2. Numerical method. We now extend the PCCU scheme developed in section 2.2 to the shallow water MHD system.

Following the notation from section 2.2, the semidiscrete PCCU scheme still reads as (2.11)–(2.12), and the resulting system of ODEs is to be numerically integrated using an appropriate ODE solver, for instance, the three-stage third-order SSP Runge–Kutta method, which we have used in the numerical experiments reported in section 3.3.

In sections 3.2.1, 3.2.2, and 3.2.3 below, we focus on details of the scheme, which are different from the ideal MHD case.

3.2.1. Piecewise linear reconstruction. A piecewise linear reconstruction is performed for the discrete variables

$$\boldsymbol{W}_{j,k} := (\overline{h}_{j,k}, u_{j,k}, v_{j,k}, (\overline{ha})_{j,k}, (\overline{hb})_{j,k}, \overline{A}_{j,k}, \overline{B}_{j,k})^\top,$$

where $u_{j,k} := {}^{(\overline{hu})_{j,k}}\!/_{\overline{h}_{j,k}}$ and $v_{j,k} := {}^{\overline{hv})_{j,k}}\!/_{\overline{h}_{j,k}}$. We then calculate cell interface values $\boldsymbol{W}_{j,k}^{\mathrm{E,\,W,\,N,\,S}}$ using (2.15). The slopes $(W_x^{(i)})_{j,k}$ for $i \neq 4$ and $(W_y^{(i)})_{j,k}$ for $i \neq 5$ are computed using the generalized minmod limiter as in (2.16)–(2.17).

As in the ideal MHD case, the slopes $((ha)_x)_{j,k}$ and $((hb)_y)_{j,k}$ are computed in a way that allows one to enforce the local discrete divergence-free condition $((ha)_x)_{j,k} + ((hb)_y)_{j,k} \equiv 0$ for all j, k. To this end, we proceed as in section 2.2.1 and set

$$((ha)_x)_{j,k} = \sigma_{j,k}\,\overline{A}_{j,k}, \quad ((hb)_y)_{j,k} = \sigma_{j,k}\,\overline{B}_{j,k},$$

where

$$\sigma_{j,k} = \min\Big\{1, \sigma_{j,k}^x, \sigma_{j,k}^y\Big\},$$

$$\sigma_{j,k}^x := \begin{cases} \min\Big\{1, \dfrac{((\widehat{ha})_x)_{j,k}}{\overline{A}_{j,k}}\Big\} & \text{if } ((\widehat{ha})_x)_{j,k}\,\overline{A}_{j,k} > 0, \\ 0 & \text{otherwise,} \end{cases}$$

$$\sigma_{j,k}^y := \begin{cases} \min\Big\{1, \dfrac{((\widehat{hb})_y)_{j,k}}{\overline{B}_{j,k}}\Big\} & \text{if } ((\widehat{hb})_y)_{j,k}\,\overline{B}_{j,k} > 0, \\ 0 & \text{otherwise,} \end{cases}$$

and $((\widehat{ha})_x)_{j,k}$ and $((\widehat{hb})_y)_{j,k}$ are computed using the generalized minmod reconstruction as in (2.16)–(2.17).

3.2.2. One-sided speeds of propagation. We point out that in the shallow water MHD case, computing the one-sided speeds $s^{\pm}_{j+\frac12,k}$ and $s^{\pm}_{j,k+\frac12}$ needed in the semidiscretization (2.11)–(2.12), is significantly easier than in the ideal MHD case. We follow the general recipe and estimate the x- and y-directional speeds using the largest and smallest eigenvalues of the matrices $\frac{\partial \boldsymbol{F}}{\partial \boldsymbol{U}}(\boldsymbol{U})-Q(\boldsymbol{U})$ and $\frac{\partial \boldsymbol{G}}{\partial \boldsymbol{U}}(\boldsymbol{U})-R(\boldsymbol{U})$, respectively. This results in

$$
\begin{aligned}
s^{+}_{j+\frac12,k}&=\max\left\{u^{\rm E}_{j,k}+\sqrt{\left(a^{\rm E}_{j,k}\right)^2+gh^{\rm E}_{j,k}},\,u^{\rm W}_{j+1,k}+\sqrt{\left(a^{\rm W}_{j+1,k}\right)^2+gh^{\rm W}_{j+1,k}},\,0\right\},\\
s^{-}_{j+\frac12,k}&=\min\left\{u^{\rm E}_{j,k}-\sqrt{\left(a^{\rm E}_{j,k}\right)^2+gh^{\rm E}_{j,k}},\,u^{\rm W}_{j+1,k}-\sqrt{\left(a^{\rm W}_{j+1,k}\right)^2+gh^{\rm W}_{j+1,k}},\,0\right\},\\
s^{+}_{j,k+\frac12}&=\max\left\{v^{\rm N}_{j,k}+\sqrt{\left(b^{\rm N}_{j,k}\right)^2+gh^{\rm N}_{j,k}},\,v^{\rm S}_{j,k+1}+\sqrt{\left(b^{\rm S}_{j,k+1}\right)^2+gh^{\rm S}_{j,k+1}},\,0\right\},\\
s^{-}_{j,k+\frac12}&=\min\left\{v^{\rm N}_{j,k}-\sqrt{\left(b^{\rm N}_{j,k}\right)^2+gh^{\rm N}_{j,k}},\,v^{\rm S}_{j,k+1}-\sqrt{\left(b^{\rm S}_{j,k+1}\right)^2+gh^{\rm S}_{j,k+1}},\,0\right\}.
\end{aligned}
$$

3.2.3. Discretization of nonconservative products. In order to evaluate the contribution of the nonconservative terms $Q(\boldsymbol{U})\boldsymbol{U}_x$ appearing on the RHS of (3.4), we again follow along the lines of [8, 11] and evaluate the corresponding integrals exactly:

$$
\begin{aligned}
&Q^{(1)}_{j,k}=Q^{(6)}_{j,k}=Q^{(7)}_{j,k}=Q^{(1)}_{\boldsymbol{\Psi},j+\frac12,k}=Q^{(6)}_{\boldsymbol{\Psi},j+\frac12,k}=Q^{(7)}_{\boldsymbol{\Psi},j+\frac12,k}=0,\\
&Q^{(2)}_{j,k}=-\int_{x_{j-\frac12}}^{x_{j+\frac12}}\frac{\widetilde{ha}(x,y_k)}{\widetilde{h}(x,y_k)}((ha)_x)_{j,k}\,{\rm d}x\\
&\qquad=\begin{cases}
-a_{j,k}\sigma_{j,k}\,\overline{A}_{j,k}\Delta x, & (h_x)_{j,k}=0,\\
-\sigma_{j,k}\,\overline{A}_{j,k}\left(\dfrac{(\overline{ha})_{j,k}(h_x)_{j,k}-\overline{h}_{j,k}\sigma_{j,k}\,\overline{A}_{j,k}}{((h_x)_{j,k})^2}\,\ln\left(\dfrac{h^{\rm E}_{j,k}}{h^{\rm W}_{j,k}}\right)\right.\\
\qquad\qquad\left.+\dfrac{\sigma_{j,k}\,\overline{A}_{j,k}\Delta x}{(h_x)_{j,k}}\right) & \text{otherwise},
\end{cases}\\
&Q^{(3)}_{j,k}=-\int_{x_{j-\frac12}}^{x_{j+\frac12}}\frac{\widetilde{hb}(x,y_k)}{\widetilde{h}(x,y_k)}((ha)_x)_{j,k}\,{\rm d}x\\
&\qquad=\begin{cases}
-b_{j,k}\sigma_{j,k}\,\overline{A}_{j,k}\Delta x, & (h_x)_{j,k}=0,\\
-\sigma_{j,k}\,\overline{A}_{j,k}\left(\dfrac{(\overline{hb})_{j,k}(h_x)_{j,k}-\overline{h}_{j,k}((hb)_x)_{j,k}}{((h_x)_{j,k})^2}\,\ln\left(\dfrac{h^{\rm E}_{j,k}}{h^{\rm W}_{j,k}}\right)\right.\\
\qquad\qquad\left.+\dfrac{((hb)_x)_{j,k}\Delta x}{(h_x)_{j,k}}\right) & \text{otherwise},
\end{cases}\\
&Q^{(4)}_{j,k}=-\int_{x_{j-\frac12}}^{x_{j+\frac12}}\widetilde{u}(x,y_k)((ha)_x)_{j,k}\,{\rm d}x=-u_{j,k}\sigma_{j,k}\,\overline{A}_{j,k}\Delta x,\\
&Q^{(5)}_{j,k}=-\int_{x_{j-\frac12}}^{x_{j+\frac12}}\widetilde{v}(x,y_k)((ha)_x)_{j,k}\,{\rm d}x=-v_{j,k}\sigma_{j,k}\,\overline{A}_{j,k}\Delta x,
\end{aligned}
$$

$$Q^{(2)}_{\boldsymbol{\Psi},j+\frac12,k} = -\int_0^1 \frac{(ha)^{\mathrm{E}}_{j,k} + s\Big((ha)^{\mathrm{W}}_{j+1,k} - (ha)^{\mathrm{E}}_{j,k}\Big)}{h^{\mathrm{E}}_{j,k} + s\Big(h^{\mathrm{W}}_{j+1,k} - h^{\mathrm{E}}_{j,k}\Big)}[ha]_{j+\frac12,k}\,\mathrm{d}s$$

$$= \begin{cases} -\dfrac{1}{2}\left(a^{\mathrm{E}}_{j,k} + a^{\mathrm{W}}_{j+1,k}\right)[ha]_{j+\frac12,k}, & [h]_{j+\frac12,k} = 0, \\ -[ha]_{j+\frac12,k}\left(\dfrac{(ha)^{\mathrm{E}}_{j,k}[h]_{j+\frac12,k} - h^{\mathrm{E}}_{j,k}[ha]_{j+\frac12,k}}{[h]^2_{j+\frac12,k}}\ln\left(\dfrac{h^{\mathrm{W}}_{j+1,k}}{h^{\mathrm{E}}_{j,k}}\right)\right. & \\ \qquad\left. + \dfrac{[ha]_{j+\frac12,k}}{[h]_{j+\frac12,k}}\right) & \text{otherwise}, \end{cases}$$

$$Q^{(3)}_{\boldsymbol{\Psi},j+\frac12,k} = -\int_0^1 \frac{(hb)^{\mathrm{E}}_{j,k} + s\Big((hb)^{\mathrm{W}}_{j+1,k} - (hb)^{\mathrm{E}}_{j,k}\Big)}{h^{\mathrm{E}}_{j,k} + s\Big(h^{\mathrm{W}}_{j+1,k} - h^{\mathrm{E}}_{j,k}\Big)}[ha]_{j+\frac12,k}\,\mathrm{d}s$$

$$= \begin{cases} -\dfrac{1}{2}\left(b^{\mathrm{E}}_{j,k} + b^{\mathrm{W}}_{j+1,k}\right)[ha]_{j+\frac12,k}, & [h]_{j+\frac12,k} = 0, \\ -[ha]_{j+\frac12,k}\left(\dfrac{(hb)^{\mathrm{E}}_{j,k}[h]_{j+\frac12,k} - h^{\mathrm{E}}_{j,k}[hb]_{j+\frac12,k}}{[h]^2_{j+\frac12,k}}\ln\left(\dfrac{h^{\mathrm{W}}_{j+1,k}}{h^{\mathrm{E}}_{j,k}}\right)\right. & \\ \qquad\left. + \dfrac{[hb]_{j+\frac12,k}}{[h]_{j+\frac12,k}}\right) & \text{otherwise}, \end{cases}$$

$$Q^{(4)}_{\boldsymbol{\Psi},j+\frac12,k} = -\int_0^1 \left\{u^{\mathrm{E}}_{j,k} + s\big(u^{\mathrm{W}}_{j+1,k} - u^{\mathrm{E}}_{j,k}\big)\right\}[ha]_{j+\frac12,k}\,\mathrm{d}s = -\frac{u^{\mathrm{E}}_{j,k} + u^{\mathrm{W}}_{j+1,k}}{2}[ha]_{j+\frac12,k},$$

$$Q^{(5)}_{\boldsymbol{\Psi},j+\frac12,k} = -\int_0^1 \left\{v^{\mathrm{E}}_{j,k} + s\big(v^{\mathrm{W}}_{j+1,k} - v^{\mathrm{E}}_{j,k}\big)\right\}[ha]_{j+\frac12,k}\,\mathrm{d}s = -\frac{v^{\mathrm{E}}_{j,k} + v^{\mathrm{W}}_{j+1,k}}{2}[ha]_{j+\frac12,k},$$

where

$$a_{j,k} := \frac{(\overline{ha})_{j,k}}{\overline{h}_{j,k}}, \quad b_{j,k} := \frac{(\overline{hb})_{j,k}}{\overline{h}_{j,k}}, \quad a^{\mathrm{E(W)}}_{j,k} := \frac{(ha)^{\mathrm{E(W)}}_{j,k}}{h^{\mathrm{E(W)}}_{j,k}}, \quad b^{\mathrm{E(W)}}_{j,k} := \frac{(hb)^{\mathrm{E(W)}}_{j,k}}{h^{\mathrm{E(W)}}_{j,k}},$$
$$[h]_{j+\frac12,k} := h^{\mathrm{W}}_{j+1,k} - h^{\mathrm{E}}_{j,k}, \quad [ha]_{j+\frac12,k} := (ha)^{\mathrm{W}}_{j+1,k} - (ha)^{\mathrm{E}}_{j,k},$$
$$[hb]_{j+\frac12,k} := (hb)^{\mathrm{W}}_{j+1,k} - (hb)^{\mathrm{E}}_{j,k}.$$

The contribution of the nonconservative terms $R(\boldsymbol{U})\boldsymbol{U}_x$ appearing on the RHS of (3.4) is obtained in a similar manner and given by

$$R^{(1)}_{j,k} = R^{(6)}_{j,k} = R^{(7)}_{j,k} = R^{(1)}_{\boldsymbol{\Psi},j,k+\frac12} = R^{(6)}_{\boldsymbol{\Psi},j,k+\frac12} = R^{(7)}_{\boldsymbol{\Psi},j,k+\frac12} = 0,$$

$$R^{(2)}_{j,k} = \begin{cases} -a_{j,k}\sigma_{j,k}\,\overline{B}_{j,k}\Delta y, & (h_y)_{j,k} = 0, \\ -\sigma_{j,k}\,\overline{B}_{j,k}\left(\dfrac{(\overline{ha})_{j,k}(h_y)_{j,k} - \overline{h}_{j,k}((ha)_y)_{j,k}}{((h_y)_{j,k})^2}\ln\left(\dfrac{h^{\mathrm{N}}_{j,k}}{h^{\mathrm{S}}_{j,k}}\right)\right. & \\ \qquad\left. + \dfrac{((ha)_y)_{j,k}\Delta y}{(h_y)_{j,k}}\right) & \text{otherwise}, \end{cases}$$

$$R^{(3)}_{j,k} = \begin{cases} -b_{j,k}\sigma_{j,k}\,\overline{B}_{j,k}\Delta y, & (h_y)_{j,k} = 0, \\ -\sigma_{j,k}\,\overline{B}_{j,k}\left(\dfrac{(\overline{hb})_{j,k}(h_y)_{j,k} - \overline{h}_{j,k}\sigma_{j,k}\,\overline{B}_{j,k}}{((h_y)_{j,k})^2}\ln\left(\dfrac{h^{\mathrm{N}}_{j,k}}{h^{\mathrm{S}}_{j,k}}\right)\right. & \\ \qquad\left. + \dfrac{\sigma_{j,k}\,\overline{B}_{j,k}\Delta y}{(h_y)_{j,k}}\right) & \text{otherwise}, \end{cases}$$

$$R^{(4)}_{j,k}=-u_{j,k}\sigma_{j,k}\,\overline{B}_{j,k}\Delta y,\quad R^{(5)}_{j,k}=-v_{j,k}\sigma_{j,k}\,\overline{B}_{j,k}\Delta y,$$

$$R^{(2)}_{\mathbf{\Psi},j,k+\frac12}=\begin{cases}-\dfrac12\left(a^{\rm N}_{j,k}+a^{\rm S}_{j,k+1}\right)[hb]_{j,k+\frac12}, & [h]_{j,k+\frac12}=0,\\ -[hb]_{j,k+\frac12}\left(\dfrac{(ha)^{\rm N}_{j,k}[h]_{j,k+\frac12}-h^{\rm N}_{j,k}[ha]_{j,k+\frac12}}{[h]^2_{j,k+\frac12}}\ln\left(\dfrac{h^{\rm S}_{j,k+1}}{h^{\rm N}_{j,k}}\right)\right.\\ \qquad\left.+\dfrac{[ha]_{j,k+\frac12}}{[h]_{j,k+\frac12}}\right) & \text{otherwise},\end{cases}$$

$$R^{(3)}_{\mathbf{\Psi},j,k+\frac12}=\begin{cases}-\dfrac12\left(b^{\rm N}_{j,k}+b^{\rm S}_{j,k+1}\right)[hb]_{j,k+\frac12}, & [h]_{j,k+\frac12}=0,\\ -[hb]_{j,k+\frac12}\left(\dfrac{(hb)^{\rm N}_{j,k}[h]_{j,k+\frac12}-h^{\rm N}_{j,k}[hb]_{j,k+\frac12}}{[h]^2_{j,k+\frac12}}\ln\left(\dfrac{h^{\rm S}_{j,k+1}}{h^{\rm N}_{j,k}}\right)\right.\\ \qquad\left.+\dfrac{[hb]_{j,k+\frac12}}{[h]_{j,k+\frac12}}\right) & \text{otherwise},\end{cases}$$

$$R^{(4)}_{\mathbf{\Psi},j,k+\frac12}=-\frac12\left(u^{\rm N}_{j,k}+u^{\rm S}_{j,k+1}\right)[hb]_{j,k+\frac12},\quad R^{(5)}_{\mathbf{\Psi},j,k+\frac12}=-\frac12\left(v^{\rm N}_{j,k}+v^{\rm S}_{j,k+1}\right)[hb]_{j,k+\frac12},$$

where

$$a^{\rm N(S)}_{j,k}:=\frac{(ha)^{\rm N(S)}_{j,k}}{h^{\rm N(S)}_{j,k}},\quad b^{\rm N(S)}_{j,k}:=\frac{(hb)^{\rm N(S)}_{j,k}}{h^{\rm N(S)}_{j,k}},\quad [h]_{j,k+\frac12}:=h^{\rm S}_{j,k+1}-h^{\rm N}_{j,k},$$
$$[ha]_{j,k+\frac12}:=(ha)^{\rm S}_{j,k+1}-(ha)^{\rm N}_{j,k},\quad [hb]_{j,k+\frac12}:=(hb)^{\rm S}_{j,k+1}-(hb)^{\rm N}_{j,k}.$$

3.3. Numerical examples. In this section, we apply the proposed PCCU scheme to the 2-D shallow water MHD equations. In all of the examples, the CFL number is set to $\eta=0.25$ to satisfy the CFL condition in (2.13), and the minmod parameter is set to $\theta=1.3$.

Example 6*—Orszag–Tang-like problem.* This example, taken from [18, 70], is similar to that of the ideal MHD Orszag–Tang problem studied in Example 3.

The shallow water MHD system is considered in the domain $[0,2\pi]\times[0,2\pi]$ subject to the periodic boundary conditions in both the x- and y-directions and the following smooth initial data:

$$(h,u,v,a,b)(x,y,0)=\left(\frac{25}{9},-\sin y,\sin x,-\sin y,\sin(2x)\right).$$

We compute the numerical solution by the proposed PCCU scheme on a uniform 200×200 mesh until the final time $t=2$. Time snapshots of h and $\sqrt{a^2+b^2}$ at $t=1$ and 2 are plotted in Figure 3.1. As one can see, the initially smooth solution breaks down and develops multiple shock waves, whose interaction leads to the appearance of many essential features of MHD turbulence. We observe that the obtained results are in good agreement with those reported in [18, 70].

Example 7*—rotor-like problem.* Next, we consider a rotor-like problem taken from [18, 33]. This benchmark, which is an extension of the ideal MHD rotor problem studied in Example 4, portrays a disk with radius 0.1 of significant fluid depth h rotating in a magnetic field.

The initial data

$$(h,u,v,ha,hb)=\begin{cases}(10,-y,x,1,0), & \sqrt{x^2+y^2}<0.1,\\ (1,0,0,1,0) & \text{otherwise}\end{cases}$$

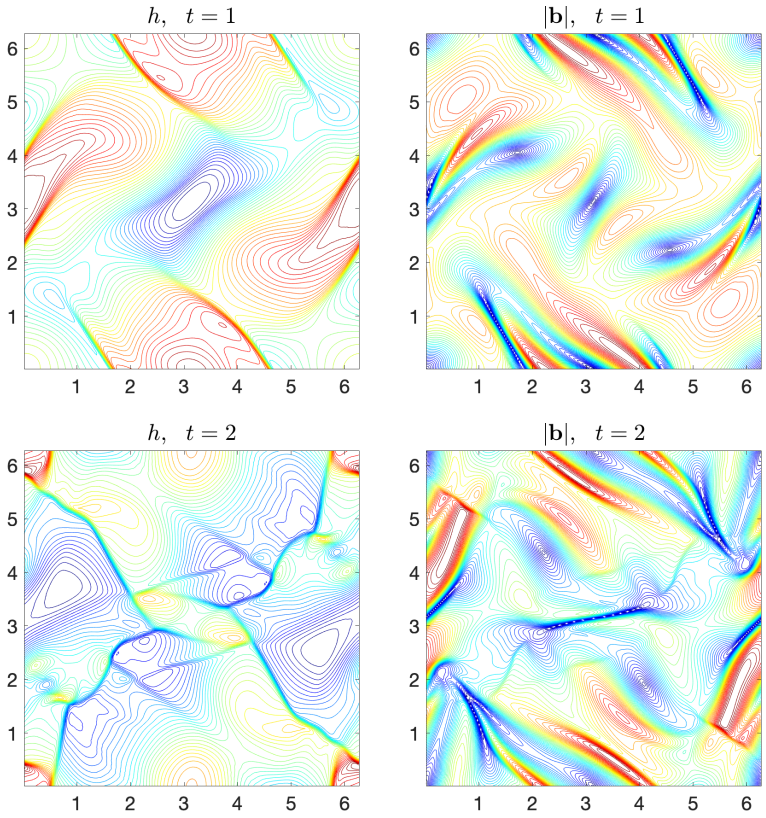

FIG. 3.1. *Example* 6: *Fluid thickness* h *and magnetic field magnitude* $\sqrt{a^2+b^2}$ *computed by the proposed PCCU scheme at* $t=1$ *(top row) and* 2 *(bottom row).* 40 *equally spaced contours are used in each plot.*

are prescribed in the computational domain $[-1,1]\times[-1,1]$, and zero-order extrapolation boundary conditions are set along its boundary. The solution computed by the proposed PCCU scheme on a uniform 200×200 mesh at time $t=0.2$ is plotted in Figure 3.2. The obtained results are oscillation-free and overall comparable to those reported in [18, 33].

Example 8—*explosion problem.* In the final example, we numerically solve the explosion problem studied in [33, 59]. This is another benchmark for the shallow water MHD equations considered subject to the following initial data:

$$(h,u,v,a,b)(x,y,0)=\begin{cases}(1,0,0,0.1,0), & \sqrt{x^2+y^2}<0.3,\\ (0.1,0,0,1,0) & \text{otherwise.}\end{cases}$$

In this example, we take the computational domain $[-1,1]\times[-1,1]$ and implement the zero-order extrapolation boundary conditions along its boundary.

The solution of the explosion problem consists of a shock traveling away from the center, a rarefaction wave traveling toward the origin, and two Alfvén waves. We compute the solution by the proposed PCCU scheme on a uniform 200×200 mesh. The obtained results, shown in Figure 3.3 at $t=0.25$, are nonoscillatory and agree well with the corresponding results in [33, 59].

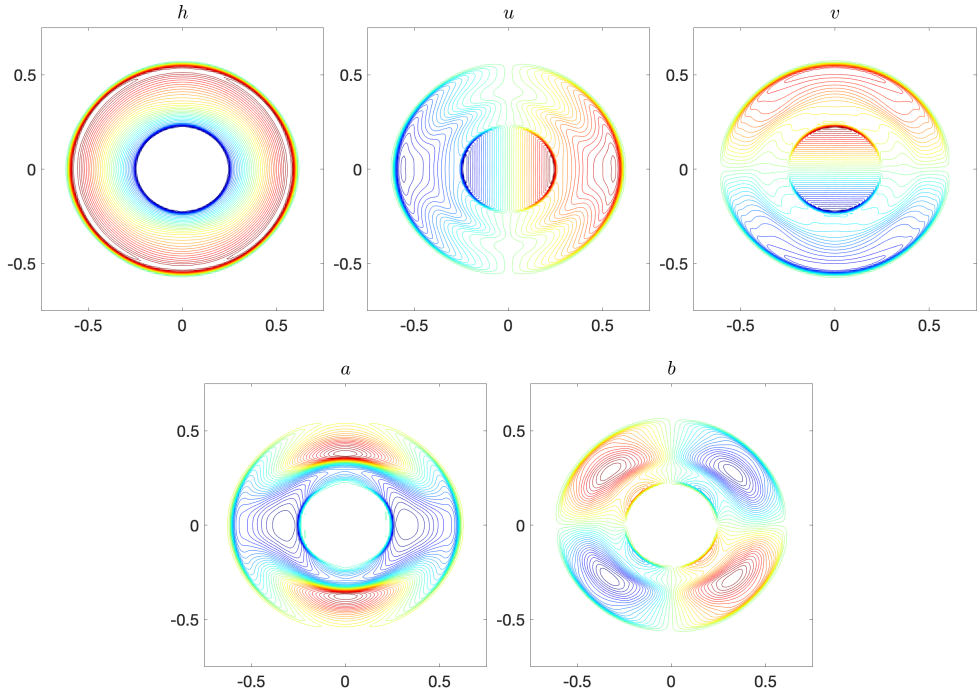

FIG. 3.2. *Example* 7: *Fluid thickness* h, *velocities* u *and* v, *and reduced magnetic field components* a *and* b *computed by the proposed PCCU scheme.* 40 *equally spaced contours are used in each plot.*

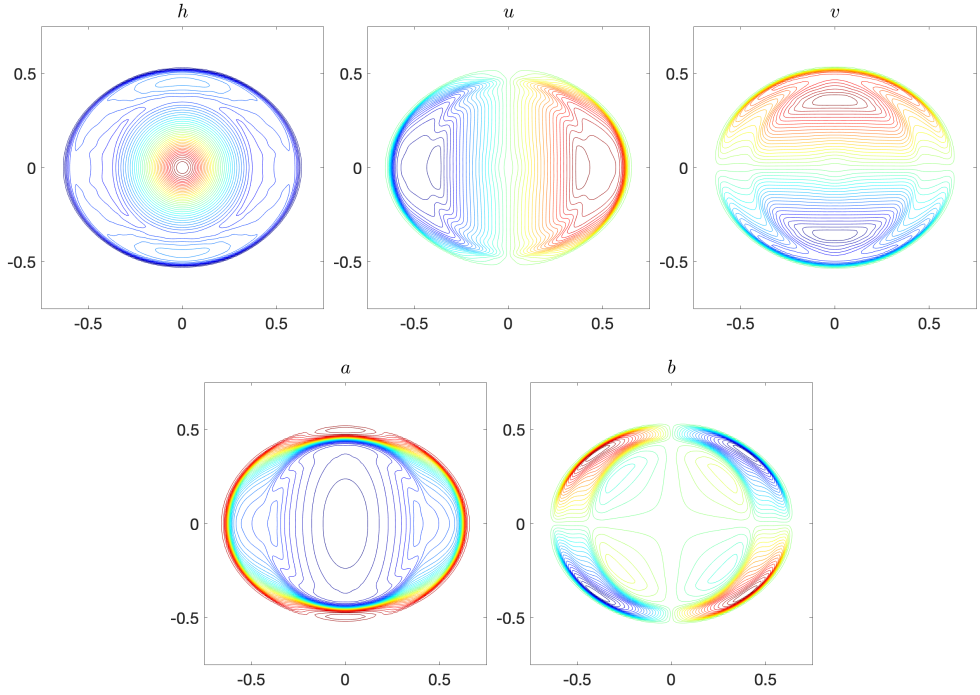

FIG. 3.3. *Example* 8: *Fluid thickness* h, *velocities* u *and* v, *and reduced magnetic field components* a *and* b *computed by the proposed PCCU scheme.* 40 *equally spaced contours are used in each plot.*

4. Conclusion. In this paper, we have developed a new second-order unstaggered path-conservative central-upwind (PCCU) scheme for the ideal and shallow water magnetohydrodynamic (MHD) systems. The proposed scheme is (i) locally divergence-free; (ii) Riemann-problem-solver-free; (iii) high-resolution; (iv) robust; and (v) nonoscillatory. The derivation of the scheme is based on the Godunov–Powell nonconservative modifications of the studied MHD systems. The local divergence-free property is enforced by augmenting the studied systems with the evolution equations for the corresponding derivatives of the magnetic field components and by using these evolved quantities in the design of a special piecewise linear reconstruction of the magnetic field, which also guarantees a nonoscillatory nature of the resulting scheme. In addition, the proposed PCCU scheme allows for a proper treatment of the nonconservative product terms, which takes into account jumps of the normal component of the magnetic field across cell interfaces, thus providing stability. The performance of the new scheme has been illustrated on several benchmarks for both ideal and shallow water MHD systems, producing high-resolution and oscillation-free results with positive computed quantities such as density, pressure, and water depth.

In future work, we plan to develop a provably positivity-preserving high-order PCCU scheme as well as introduce a new well-balanced PCCU scheme for more general shallow water MHD systems with the nonflat bottom topography and Coriolis forces taken into account.

Acknowledgment. The authors would like to express their gratitude to Prof. Vladimir Zeitlin from the Laboratory of Dynamical Meteorology, Sorbonne University, Ecole Normale Supérieure, CNRS, Paris, for motivating and fruitful discussions.

REFERENCES

[1] S. Ahmed and S. Zia, *The higher-order CESE method for two-dimensional shallow water magnetohydrodynamics equations*, Eur. J. Pure Appl. Math., 12 (2019), pp. 1464–1482.

[2] D. S. Balsara, *Divergence-free reconstruction of magnetic fields and WENO schemes for magnetohydrodynamics*, J. Comput. Phys., 228 (2009), pp. 5040–5056.

[3] D. S. Balsara, R. Kumar, and P. Chandrashekar, *Globally divergence-free DG scheme for ideal compressible MHD*, Commun. Appl. Math. Comput. Sci., 16 (2021), pp. 59–98.

[4] D. S. Balsara, T. Rumpf, M. Dumbser, and C.-D. Munz, *Efficient, high accuracy ADER-WENO schemes for hydrodynamics and divergence-free magnetohydrodynamics*, J. Comput. Phys., 228 (2009), pp. 2480–2516.

[5] D. S. Balsara and D. S. Spicer, *A staggered mesh algorithm using high order Godunov fluxes to ensure solenoidal magnetic fields in magnetohydrodynamic simulations*, J. Comput. Phys., 149 (1999), pp. 270–292.

[6] J. U. Brackbill and D. C. Barnes, *The effect of nonzero $\nabla \cdot B$ on the numerical solution of the magnetohydrodynamic equations*, J. Comput. Phys., 35 (1980), pp. 426–430.

[7] M. Brio and C. C. Wu, *An upwind differencing scheme for the equations of ideal magnetohydrodynamics*, J. Comput. Phys., 75 (1988), pp. 400–422.

[8] M. J. Castro Díaz, A. Kurganov, and T. Morales de Luna, *Path-conservative central-upwind schemes for nonconservative hyperbolic systems*, ESAIM Math. Model. Numer. Anal., 53 (2019), pp. 959–985.

[9] P. Chandrashekar and C. Klingenberg, *Entropy stable finite volume scheme for ideal compressible MHD on 2-D Cartesian meshes*, SIAM J. Numer. Anal., 54 (2016), pp. 1313–1340, https://doi.org/10.1137/15M1013626.

[10] A. J. Christlieb, J. A. Rossmanith, and Q. Tang, *Finite difference weighted essentially non-oscillatory schemes with constrained transport for ideal magnetohydrodynamics*, J. Comput. Phys., 268 (2014), pp. 302–325.

[11] S. Chu, A. Kurganov, and M. Na, *Fifth-order A-WENO schemes based on the path-conservative central-upwind method*, J. Comput. Phys., 469 (2022), 111508.

[12] W. Dai and P. R. Woodward, *A simple finite difference scheme for multidimensional magnetohydrodynamical equations*, J. Comput. Phys., 142 (1998), pp. 331–369.

[13] A. Dedner, F. Kemm, D. Kröner, C.-D. Munz, T. Schnitzer, and M. Wesenberg, *Hyperbolic divergence cleaning for the MHD equations*, J. Comput. Phys., 175 (2002), pp. 645–673.
[14] P. J. Dellar, *A note on magnetic monopoles and the one-dimensional MHD Riemann problem*, J. Comput. Phys., 172 (2001), pp. 392–398.
[15] P. J. Dellar, *Dispersive shallow water magnetohydrodynamics*, Phys. Plasmas, 10 (2003), pp. 581–590.
[16] D. Derigs, G. J. Gassner, S. Walch, and A. R. Winters, *Entropy stable finite volume approximations for ideal magnetohydrodynamics*, Jahresber. Dtsch. Math.-Ver., 120 (2018), pp. 153–219.
[17] C. R. DeVore, *Flux-corrected transport techniques for multidimensional compressible magnetohydrodynamics*, J. Comput. Phys., 92 (1991), pp. 142–160.
[18] J. Duan and H. Tang, *High-order accurate entropy stable finite difference schemes for the shallow water magnetohydrodynamics*, J. Comput. Phys., 431 (2021), 110136.
[19] M. Dumbser, D. S. Balsara, M. Tavelli, and F. Fambri, *A divergence-free semi-implicit finite volume scheme for ideal, viscous, and resistive magnetohydrodynamics*, Internat. J. Numer. Methods Fluids, 89 (2019), pp. 16–42.
[20] B. Einfeldt, C.-D. Munz, P. L. Roe, and B. Sjögreen, *On Godunov-type methods near low densities*, J. Comput. Phys., 92 (1991), pp. 273–295.
[21] C. R. Evans and J. F. Hawley, *Simulation of magnetohydrodynamic flows: A constrained transport method*, Astrophys. J., 332 (1988), pp. 659–677.
[22] P. Fu, F. Li, and Y. Xu, *Globally divergence-free discontinuous Galerkin methods for ideal magnetohydrodynamic equations*, J. Sci. Comput., 77 (2018), pp. 1621–1659.
[23] F. G. Fuchs, A. D. McMurry, S. Mishra, N. H. Risebro, and K. Waagan, *Approximate Riemann solvers and robust high-order finite volume schemes for multi-dimensional ideal MHD equations*, Commun. Comput. Phys., 9 (2011), pp. 324–362.
[24] T. A. Gardiner and J. M. Stone, *An unsplit Godunov method for ideal MHD via constrained transport*, J. Comput. Phys., 205 (2005), pp. 509–539.
[25] P. A. Gilman, *Magnetohydrodynamic "shallow water" equations for the solar tachocline*, Astrophys. J. Lett., 544 (2000), pp. L79–L82.
[26] S. K. Godunov, *Symmetric form of the equations of magnetohydrodynamics*, Numer. Methods Mech. Continuum Medium, 1 (1972), pp. 26–34 (in Russian).
[27] S. Gottlieb, D. Ketcheson, and C.-W. Shu, *Strong Stability Preserving Runge-Kutta and Multistep Time Discretizations*, World Scientific, Hackensack, NJ, 2011.
[28] S. Gottlieb, C.-W. Shu, and E. Tadmor, *Strong stability-preserving high-order time discretization methods*, SIAM Rev., 43 (2001), pp. 89–112, https://doi.org/10.1137/S0036145003604036757X.
[29] C. Helzel, J. A. Rossmanith, and B. Taetz, *An unstaggered constrained transport method for the 3D ideal magnetohydrodynamic equations*, J. Comput. Phys., 230 (2011), pp. 3803–3829.
[30] C. Helzel, J. A. Rossmanith, and B. Taetz, *A high-order unstaggered constrained-transport method for the three-dimensional ideal magnetohydrodynamic equations based on the method of lines*, SIAM J. Sci. Comput., 35 (2013), pp. A623–A651, https://doi.org/10.1137/120870323.
[31] P. Janhunen, *A positive conservative method for magnetohydrodynamics based on HLL and Roe methods*, J. Comput. Phys., 160 (2000), pp. 649–661.
[32] F. Kemm, *Roe-type schemes for shallow water magnetohydrodynamics with hyperbolic divergence cleaning*, Appl. Math. Comput., 272 (2016), pp. 385–402.
[33] T. Kröger and M. Lukáčová-Medviďová, *An evolution Galerkin scheme for the shallow water magnetohydrodynamic equations in two space dimensions*, J. Comput. Phys., 206 (2005), pp. 122–149.
[34] A. Kurganov and C.-T. Lin, *On the reduction of numerical dissipation in central-upwind schemes*, Commun. Comput. Phys., 2 (2007), pp. 141–163.
[35] A. Kurganov, S. Noelle, and G. Petrova, *Semidiscrete central-upwind schemes for hyperbolic conservation laws and Hamilton–Jacobi equations*, SIAM J. Sci. Comput., 23 (2001), pp. 707–740, https://doi.org/10.1137/S1064827500373413.
[36] A. Kurganov and G. Petrova, *A second-order well-balanced positivity preserving central-upwind scheme for the Saint-Venant system*, Commun. Math. Sci., 5 (2007), pp. 133–160.
[37] A. Kurganov and E. Tadmor, *New high-resolution central schemes for nonlinear conservation laws and convection-diffusion equations*, J. Comput. Phys., 160 (2000), pp. 241–282.

[38] A. Kurganov and E. Tadmor, *Solution of two-dimensional Riemann problems for gas dynamics without Riemann problem solvers*, Numer. Methods Partial Differential Equations, 18 (2002), pp. 584–608.
[39] N. Lahaye and V. Zeitlin, *Coherent magnetic modon solutions in quasi-geostrophic shallow water magnetohydrodynamics*, J. Fluid Mech., 941 (2022), A15.
[40] F. Li and C.-W. Shu, *Locally divergence-free discontinuous Galerkin methods for MHD equations*, J. Sci. Comput., 22 (2005), pp. 413–442.
[41] F. Li and L. Xu, *Arbitrary order exactly divergence-free central discontinuous Galerkin methods for ideal MHD equations*, J. Comput. Phys., 231 (2012), pp. 2655–2675.
[42] F. Li, L. Xu, and S. Yakovlev, *Central discontinuous Galerkin methods for ideal MHD equations with the exactly divergence-free magnetic field*, J. Comput. Phys., 230 (2011), pp. 4828–4847.
[43] K.-A. Lie and S. Noelle, *On the artificial compression method for second-order nonoscillatory central difference schemes for systems of conservation laws*, SIAM J. Sci. Comput., 24 (2003), pp. 1157–1174, https://doi.org/10.1137/S1064827501392880.
[44] M. Liu, M. Zhang, C. Li, and F. Shen, *A new locally divergence-free WLS-ENO scheme based on the positivity-preserving finite volume method for ideal MHD equations*, J. Comput. Phys., 447 (2021), 110694.
[45] Y. Liu, C.-W. Shu, and M. Zhang, *Entropy stable high order discontinuous Galerkin methods for ideal compressible MHD on structured meshes*, J. Comput. Phys., 354 (2018), pp. 163–178.
[46] P. Londrillo and L. Del Zanna, *On the divergence-free condition in Godunov-type schemes for ideal magnetohydrodynamics: The upwind constrained transport method*, J. Comput. Phys., 195 (2004), pp. 17–48.
[47] S. Mishra and E. Tadmor, *Constraint preserving schemes using potential-based fluxes.* III. *Genuinely multi-dimensional schemes for MHD equations*, ESAIM Math. Model. Numer. Anal., 46 (2012), pp. 661–680.
[48] H. Nessyahu and E. Tadmor, *Nonoscillatory central differencing for hyperbolic conservation laws*, J. Comput. Phys., 87 (1990), pp. 408–463.
[49] S. A. Orszag and C.-M. Tang, *Small-scale structure of two-dimensional magnetohydrodynamic turbulence*, J. Fluid Mech., 90 (1979), pp. 129–143.
[50] A. Petrosyan, D. Klimachkov, M. Fedotova, and T. Zinyakov, *Shallow water magnetohydrodynamics in plasma astrophysics. Waves, turbulence, and zonal flows*, Atmosphere, 11 (2020), 314.
[51] K. G. Powell, *An approximate Riemann solver for magnetohydrodynamics*, in Upwind and High-Resolution Schemes, M. Y. Hussaini, B. van Leer, and J. Van Rosendale, eds., Springer, Berlin, Heidelberg, 1997, pp. 570–583.
[52] K. G. Powell, P. L. Roe, T. J. Linde, T. I. Gombosi, and D. L. De Zeeuw, *A solution-adaptive upwind scheme for ideal magnetohydrodynamics*, J. Comput. Phys., 154 (1999), pp. 284–309.
[53] K. G. Powell, P. L. Roe, R. S. Myong, T. Gombosi, and D. De Zeeuw, *An upwind scheme for magnetohydrodynamics*, in 12th Computational Fluid Dynamics Conference: AIAA Paper 95-1704-CP, AIAA, 1995, pp. 661–674.
[54] S. Qamar and G. Warnecke, *Application of space-time CE/SE method to shallow water magnetohydrodynamic equations*, J. Comput. Appl. Math., 196 (2006), pp. 132–149.
[55] J. A. Rossmanith, *An unstaggered, high-resolution constrained transport method for magnetohydrodynamic flows*, SIAM J. Sci. Comput., 28 (2006), pp. 1766–1797, https://doi.org/10.1137/050627022.
[56] D. Ryu, F. Miniati, T. W. Jones, and A. Frank, *A divergence-free upwind code for multidimensional magnetohydrodynamic flows*, Astrophys. J., 509 (1998), pp. 244–255.
[57] P. K. Sweby, *High resolution schemes using flux limiters for hyperbolic conservation laws*, SIAM J. Numer. Anal., 21 (1984), pp. 995–1011, https://doi.org/10.1137/0721062.
[58] G. Tóth, *The* $\nabla \cdot B = 0$ *constraint in shock-capturing magnetohydrodynamics codes*, J. Comput. Phys., 161 (2000), pp. 605–652.
[59] R. Touma, *Unstaggered central schemes with constrained transport treatment for ideal and shallow water magnetohydrodynamics*, Appl. Numer. Math., 60 (2010), pp. 752–766.
[60] K. Waagan, C. Federrath, and C. Klingenberg, *A robust numerical scheme for highly compressible magnetohydrodynamics: Nonlinear stability, implementation and tests*, J. Comput. Phys., 230 (2011), pp. 3331–3351.
[61] A. R. Winters and G. J. Gassner, *An entropy stable finite volume scheme for the equations of shallow water magnetohydrodynamics*, J. Sci. Comput., 67 (2016), pp. 514–539.

[62] K. Wu, *Positivity-preserving analysis of numerical schemes for ideal magnetohydrodynamics*, SIAM J. Numer. Anal., 56 (2018), pp. 2124–2147, https://doi.org/10.1137/18M1168017.
[63] K. Wu and C.-W. Shu, *A provably positive discontinuous Galerkin method for multidimensional ideal magnetohydrodynamics*, SIAM J. Sci. Comput., 40 (2018), pp. B1302–B1329, https://doi.org/10.1137/18M1168042.
[64] K. Wu and C.-W. Shu, *Provably positive high-order schemes for ideal magnetohydrodynamics: Analysis on general meshes*, Numer. Math., 142 (2019), pp. 995–1047.
[65] K. Wu and C.-W. Shu, *Geometric quasilinearization framework for analysis and design of bound-preserving schemes*, SIAM Rev., 65 (2023), pp. 1031–1073, https://doi.org/10.1137/21M1458247.
[66] Z. Xu, D. S. Balsara, and H. Du, *Divergence-free WENO reconstruction-based finite volume scheme for solving ideal MHD equations on triangular meshes*, Commun. Comput. Phys., 19 (2016), pp. 841–880.
[67] S. Yakovlev, L. Xu, and F. Li, *Locally divergence-free central discontinuous Galerkin methods for ideal MHD equations*, J. Comput. Sci., 4 (2013), pp. 80–91.
[68] V. Zeitlin, *Remarks on rotating shallow-water magnetohydrodynamics*, Nonlinear Process. Geophys., 20 (2013), pp. 893–898.
[69] V. Zeitlin, C. Lusso, and F. Bouchut, *Geostrophic vs magneto-geostrophic adjustment and nonlinear magneto-inertia-gravity waves in rotating shallow water magnetohydrodynamics*, Geophys. Astrophys. Fluid Dyn., 109 (2015), pp. 497–523.
[70] S. Zia, M. Ahmed, and S. Qamar, *Numerical solution of shallow water magnetohydrodynamic equations with non-flat bottom topography*, Int. J. Comput. Fluid Dyn., 28 (2014), pp. 56–75.